

Voltage hysteresis during lithiation/delithiation of graphite associated with meta-stable carbon stackings

Michael Mercer (✉ m.mercer1@lancaster.ac.uk)

Lancaster University <https://orcid.org/0000-0001-7578-3554>

Chao Peng

University of Southampton

Cindy Soares

Lancaster University

Harry Hoster

Lancaster University <https://orcid.org/0000-0001-6379-5275>

Denis Kramer

Faculty of Mechanical Engineering, Helmut Schmidt University <https://orcid.org/0000-0003-0605-1047>

Article

Keywords: hysteresis, graphite, lithium ion, staging, DFT, entropy, electrochemical

Posted Date: August 13th, 2020

DOI: <https://doi.org/10.21203/rs.3.rs-53631/v1>

License:  This work is licensed under a Creative Commons Attribution 4.0 International License.

[Read Full License](#)

Version of Record: A version of this preprint was published at Journal of Materials Chemistry A on January 1st, 2021. See the published version at <https://doi.org/10.1039/D0TA10403E>.

Voltage hysteresis during lithiation/delithiation of graphite associated with meta-stable carbon stackings

Michael P. Mercer^{1,2,3,*}, Chao Peng^{3,4,6}, Cindy Soares¹, Harry E. Hoster^{1,2,3}, and Denis Kramer^{3,4,5}

¹Department of Chemistry, Lancaster University, Bailrigg, Lancaster, LA1 4YB, UK

²ALISTORE European Research Institute CNRS FR 3104, Hub de l'Energie, Rue Baudelocque, 80039, Amiens, France

³The Faraday Institution, Quad One, Harwell Science and Innovation Campus, Didcot, UK

⁴School of Engineering, University of Southampton, Southampton SO17 1BJ, UK

⁵Faculty of Mechanical Engineering, Helmut-Schmidt University, Holstenhofweg 85, 22043 Hamburg, Germany

August 4, 2020

Cell voltage is a fundamental quantity used to monitor and control Li-ion batteries. The open circuit voltage (OCV) is of particular interest as it is believed to be a thermodynamic quantity, free of kinetic effects and history and, therefore, “simple” to interpret. Here we show that the OCV characteristics of graphite show hysteresis between charge and discharge that does not solely originate from Li dynamics and that the OCV is in fact history dependent. Combining First Principles calculations with temperature-controlled electrochemical measurements, we identify a residual hysteresis that persists even at elevated temperatures of greater than 50°C due to differences in the phase succession between charge and discharge. Experimental entropy profiling, as well as energies and volume changes determined from First Principles calculations, suggest that the residual hysteresis is associated with different host lattice stackings of carbon and is related to Li disorder across planes in stage II configurations.

Keywords: hysteresis, graphite, lithium ion, staging, DFT, entropy, electrochemical

corresponding author: m.mercer1@lancaster.ac.uk

⁶These authors contributed equally.

1 Introduction

Graphite is ubiquitous as the primary anode material in lithium-ion batteries and has been the subject of extensive research, because of its high capacity, long cycle life, low operating voltage and high safety. Lithium (de)intercalation in graphite proceeds through a variety of stages, denoted “Stage n ”, where n is the number of graphene layers between each lithium-filled layer [1, 2, 3, 4]. The stages are known to adopt different stackings of the carbon host lattice, as shown in Figure 1. We will utilise the nomenclature introduced elsewhere [5] to denote the carbon stacking and Li occupancies: periodic carbon layer stackings along the [001] axis are designated by uppercase letters separated by Greek lowercase letters if Li is intercalated between planes. For instance, pristine graphite ($x = 0$) is AB stacked, while fully lithiated Stage I LiC_6 ($x = 1$) adopts $\text{A}\alpha\text{A}\alpha\text{A}\alpha$ stacking [3, 6, 7]. Here α denotes a lithium filled layer and x is the fraction of Li in Li_xC_6 ($0 \leq x \leq 1$).

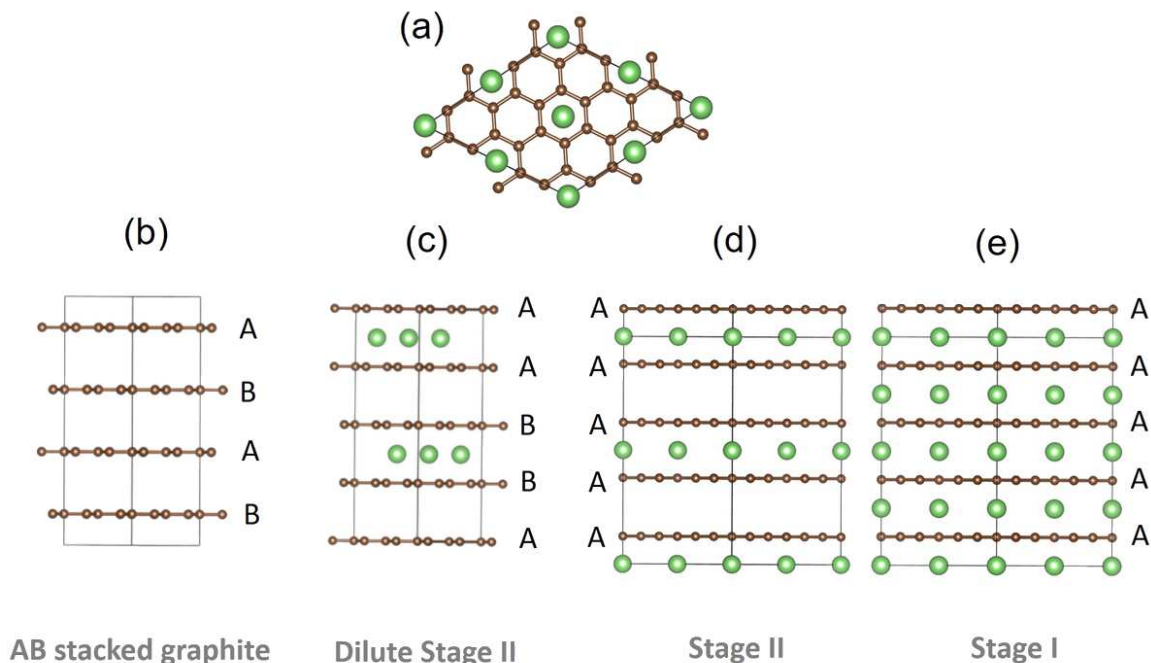


Figure 1: Structural representations of different carbon stackings in experimentally confirmed stages of graphite. (a) Top down view of carbon and lithium arrangements in Stages I and II. (b-e): side views, showing the layers occupied with Li and carbon stackings in (b) empty AB stacked graphite, (c) $A\alpha AB\beta B$ stacked dilute Stage II, with β indicating a lithium layer translated with respect to α , (d) $A\alpha AA\alpha A$ Stage II and (e) $A\alpha$ stacked Stage I. Green represent Li atoms while the brown indicate C atoms.

38 Table 1 summarises the current consensus on the stages formed during lithiation and delithiation of graphite,
 39 as obtained from *in-situ* electrochemical X-ray diffraction (XRD) and neutron diffraction [8, 9, 10, 7, 1, 2,
 40 11, 12], spectroscopic measurements [13, 14] and X-ray ex-situ analysis of compounds obtained by heat
 41 treatment [3].

Table 1: Overview of carbon stackings and stoichiometries of lithium-graphite stages from the literature.
 [15, 16, 4, 11, 17, 5, 1, 2]

Stage	Stacking	Composition x in Li_xC_6
Stage I	$A\alpha A\alpha$	$x = 1$ (LiC_6)
Stage II	$A\alpha AA\alpha A$	$x = 0.5$ (LiC_{12})
Dilute Stage II (IID)	$A\alpha AB\beta B$	$x \approx 0.33$ (LiC_{18})
Stage III	$A\alpha AB$ or $A\alpha ABA\alpha AC$	$x \approx 0.22$ (LiC_{27})
Stage IV	Unknown	$x \approx 0.167$ (LiC_{36})
Dilute Stage I (ID)	AB	$x \approx 0.0833$ (LiC_{72})
Graphite	AB	$x = 0$

42 In the higher stages III and IV proposed based on electrochemical and XRD measurements [1, 2], the host
 43 lattice stacking is still either hypothetical or disputed. Diffraction and electrochemical dQ/dV features from
 44 these stages both showed a complex temperature dependence [1, 18]. The associated XRD peaks are broader,
 45 indicating a lower degree of long range order and so those stages are considered less important for interpreting
 46 the electrochemical behaviour than those indicated in Figure 1.

47 The measured open circuit voltage (OCV) is usually considered equivalent to the equilibrium potential, which
48 is dictated by the sequence of Li/graphite stages. Measurement of the state of charge (SOC, i.e. the lithium
49 content in the electrode materials) in Battery Management Systems, for example, relies on this interpretation
50 of the OCV [19, 20]. But a hysteresis between lithiation and delithiation of the measureable OCV is generally
51 observed even for Li/graphite half cells [2, 21, 1, 22, 23, 7, 24, 12], suggesting that the full cell OCV is not a
52 simple function of the thermodynamic ground state. The lack of a clear one-to-one relationship between the
53 OCV and the state of charge could lead to incorrect battery management and control decisions, leading to
54 lithium plating and safety issues. To clarify the role of kinetics of lithiation/delithiation, versus a true path
55 dependency on the OCV hysteresis, extending the measurement relaxation time indefinitely is unfeasible.
56 Alternatively, the temperature can be varied to separate processes by activation energy. Surprisingly, the
57 temperature-dependence of the OCV over a wider range than near room temperature (i.e., 20-30°C) hasn't
58 attracted much attention yet. Varying the temperature under OCV relaxation conditions also allows the
59 entropic and enthalpic origins of the OCV hysteresis to be separated [22, 25], allowing greater understanding
60 of the physical origin of that hysteresis.

61 *First Principles* calculations, such as the cluster expansions of different Stage I and Stage II compounds
62 performed by Persson *et al.* [26], can also provide insights into the phase behaviour and kinetics of the staging
63 phenomena. However, Persson *et al.* did not explicitly consider the rearrangement of the carbon layers
64 during transitions between stages, motivating an extension of current understanding through a combined
65 experimental/theoretical approach.

66 We hypothesise that the experimentally observed OCV hysteresis between lithiation and delithiation in
67 slow continuous galvanostatic measurements and in galvanostatic intermittent titration technique (GITT)
68 experiments originates from different carbon stacking pathways during lithiation versus delithiation [11, 6,
69 27, 28]. In-situ XRD suggests Stage I - Stage II coexistence for $x \geq 0.5$ within an AAAA stacked host
70 lattice in both cycling directions [9, 8]. Previous in-situ measurements have failed to fully resolve the host
71 lattice configurations for lithium filling $x < 0.5$ [9, 8, 29]. Therefore, a combination of carefully designed
72 experiments and *ab-initio* calculations is used to substantiate this interpretation.

73 The paper is structured as follows. The measureable OCV is thoroughly characterised through GITT ex-
74 periments in both cycling directions and as a function of temperature. From the temperature dependence
75 of the OCV, we show that energetic and entropic contributions to the OCV differ depending on cycle di-
76 rection. Supported by First Principles total energy calculations, the energetic contribution is attributed to
77 carbon stacking differences, with AA-type stackings persisting for $x < 0.5$ during delithiation. The measured
78 entropic differences, on the other hand, originate from an increased amount of Li in formally empty layers
79 during delithiation resulting in additional configurational entropy.

80 The existence of meta-stable carbon stackings suggests a significant activation energy for carbon layer shifts,
81 which nudged-elastic-band calculations show to not exist in perfectly ordered Stage II configurations at
82 0 K. Rather, we propose that the levels of residual Li occupying formally empty layers alters the energy
83 landscape of carbon stackings, resulting in the persistence of meta-stable AA-type stackings for $x < 0.5$
84 during delithiation. Further evidence of a different stacking behaviour is provided by comparing previously
85 reported experimental graphite volume changes dependent on cycling direction with expected trends from
86 Density Functional Theory (DFT) calculations. The implications of these findings for understanding and
87 mitigating hysteresis, not just in graphite, but in other Li and Na-ion intercalation hosts, are discussed.

88 2 Results

89 2.1 Open circuit voltage (OCV) variation with cycle direction and temperature

90 Open circuit voltage (OCV) results from Li/graphite coin cells, as obtained with the GITT variant described
91 in section 4.4 are shown in Figure 2. The lithium content x was calculated by normalising the cumulative

92 charge passed after each galvanostatic iteration to the total charge passed during the entire experiment. The
 93 OCV measured at the end of each relaxation period is plotted against Li content x (x = Li concentration in
 94 Li_xC_6) for lithiation (Figure 2a) and delithiation (Figure 2b) at different temperatures T . The same results
 are plotted in Figure 2c-f at fixed temperatures, with lithiation and delithiation overlaid.

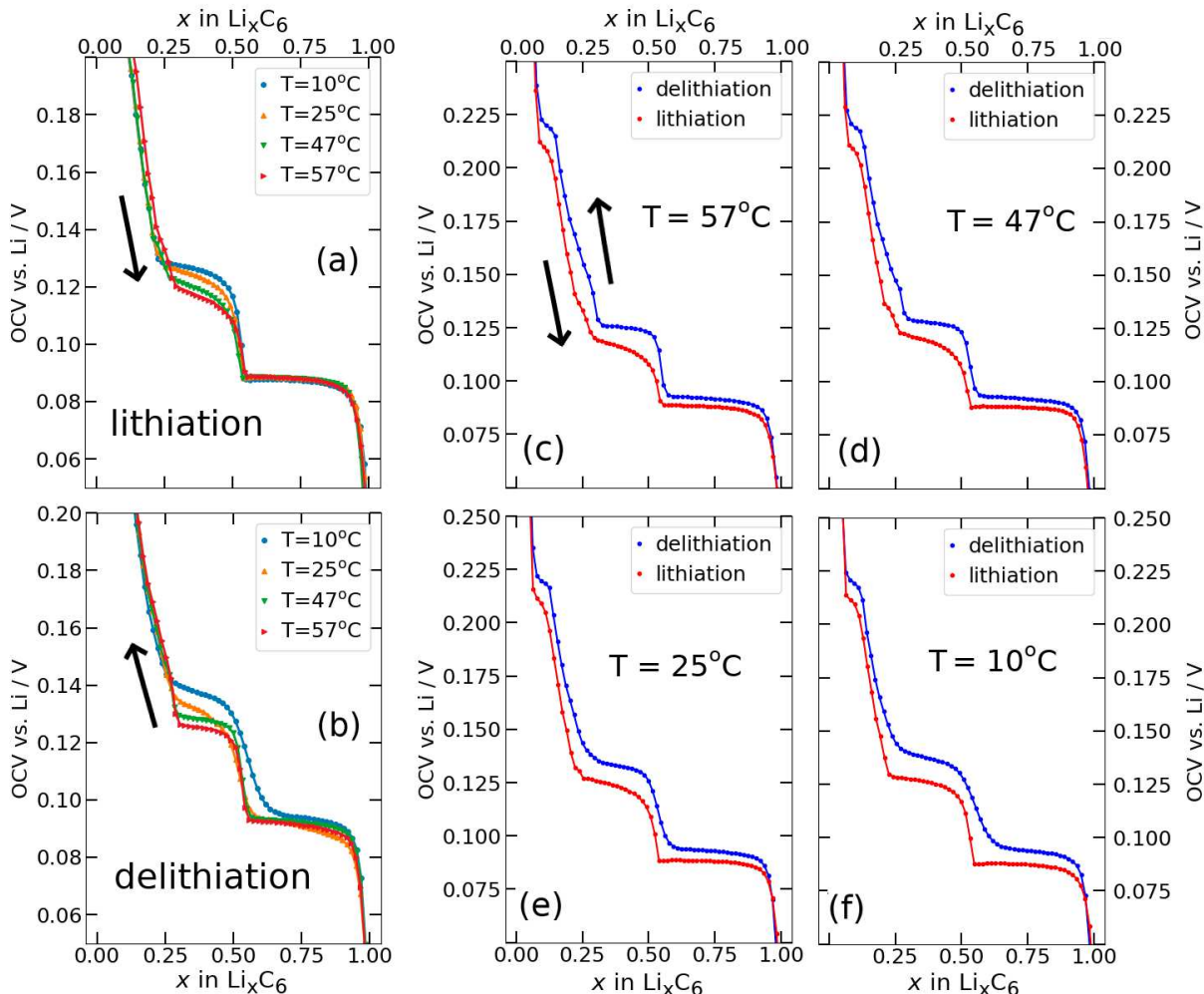


Figure 2: Experimental GITT results for (a) lithiation and (b) delithiation, at different temperatures, where the central cell temperature T_c is presented in the legend. Arrows indicate the direction of cycling. (c-f): the same results shown at fixed temperatures, in order of descending temperature (as indicated), with lithiation and delithiation overlaid.

95

96 The electrochemical OCV behaviour at $T = 25^\circ \pm 5^\circ\text{C}$, has been well characterised elsewhere [14, 21, 8, 9,
 97 22, 13, 30, 1, 2] and our results are in good agreement. Briefly: a Stage I solid solution occurs for $x > 0.85$.
 98 The interval $0.5 \leq x \leq 0.85$ is ascribed to Stage I-Stage II coexistence [1, 11, 2, 8, 9, 14, 29], with the flat
 99 voltage response typical for a two-phase equilibrium. The observed step at $x = 0.5$ is proposed to arise from
 100 a transition from an ordered Stage II to a disordered Stage IID [31, 32, 33, 34, 35]. The voltage behaviour
 101 for $0.3 \leq x \leq 0.5$ is ascribed to Stage II and dilute Stage II coexistence [11, 1, 3]. Dilute higher order stages
 102 III and IV [1, 2] approximating the behaviour of a solid solution, give rise to the observed behaviour for

103 $x < 0.3$.

104 Most of the lithiation profile (Figure 2a) is rather insensitive to temperature changes. In particular, the
105 plateau at about 0.085 V in the interval $0.5 < x < 1.0$, shows negligible variation with temperature, as
106 expected for a first order phase transition. Likewise, there is no significant change of the measured OCV
107 with temperature for $x < 0.25$. However, the interval $0.25 < x < 0.5$ shows a systematic decrease in cell
108 voltage with increasing cell temperature. Delithiation profiles, shown in Figure 2b, display a more complex
109 temperature dependence than the lithiation profiles. However, both data sets show a decrease in cell voltage
110 with increasing temperature. We return to this point in section 2.2.

111 The step at about $x = 0.5$ remains well defined above room temperature, and the change in OCV with
112 temperature reflects the same trend as observed for lithiation: a decrease in OCV only in the interval
113 $0.25 < x < 0.5$. At and below room temperature, however, the profiles are sensitive to temperature over
114 a broader range of x . In particular, the feature at $x = 0.5$ becomes much broader and extends further to
115 higher lithium content.

116 Figure 2c-f show that a hysteresis of the measured OCV between lithiation and delithiation, respectively, is
117 observed at all investigated temperatures. The hysteresis is smallest in the composition range $0.5 < x < 1.0$,
118 where the two curves appear to converge towards the same value of OCV with an increase in temperature.
119 The voltage separation between lithiation and delithiation is lowest at the highest temperature, Figure 2c,
120 between $0.5 < x < 1$, and then increases with lower temperatures.

121 The most important result for the subsequent analysis is that the hysteresis between lithiation and delithia-
122 tion remains pronounced even at $T = 57^\circ\text{C}$ for $x < 0.5$. For these compositions, a plateau is observed
123 during delithiation that appears more clearly resolved at higher temperatures and broadens out at lower
124 temperatures. A plateau is also observed during lithiation (Figure 2f) in the same composition interval that
125 appears most defined at the lowest temperature and loses definition with an increase in temperature.

126 2.2 Dependence of entropy and enthalpy profiles on cycle direction

127 Partial molar (p.m.) entropy and enthalpy profiles, acquired using the procedure described in section 4.4
128 are presented in Figure 3a-b. Results were obtained by modifying the cell temperature during the OCV
129 relaxation period for each x value and determining partial molar (p.m.) enthalpy (Figure 3a) and p.m.
130 entropy (Figure 3b) by equations 8 and 7, respectively. The corresponding OCV profiles at the end of the
131 relaxation periods are shown in Figure 3c. Results are shown in Figure 3 such that addition of the upper
132 two curves gives $-\partial G/\partial x$ (i.e. the OCV) in the lower curve.

133 Results obtained during lithiation, shown in Figure 3a-b, are in good agreement with those obtained elsewhere
134 by Reynier and Yazami [32, 33, 7], Thomas and Newman [36], and us [31]. Key features of the lithiation
135 profiles, labelled from right to left as **1-5** in Figure 3a, are commonly interpreted according to the phase
136 succession already discussed: **1**: Stage I solid solution; **2**: Stage I-Stage II coexistence; **3**: a transition from
137 ordered Stage II structure at $x = 0.5$ to a disordered dilute Stage II for $x < 0.5$ [7, 32, 33, 31]; **4**: Stage II -
138 dilute Stage II coexistence; **5**: a dilute feature at low Li occupation [31] that shows a p.m. entropy response
139 approximating a solid solution and appears to have a distinct origin from a phase transition [31]. Further
140 interpretation of the entropy profile features is in the Supplementary Information, Figure S4.

141 There is a pronounced difference in entropy responses between lithiation and delithiation for $x < 0.5$ as
142 previously observed by Allart *et al.* [22]. The negative p.m. entropy value in this interval, for both cycling
143 directions, is also consistent with the observed decrease in OCV with increasing cell temperature, as shown
144 in Figure 2. Additionally, there is a difference between the enthalpy profiles obtained from the two cycling
145 directions, Figure 3a, suggesting there is both an entropy and an enthalpy component to the hysteresis over
146 a wide range of composition $0.1 < x < 0.5$.

147 Feature **4** in Figure 3a shows a local maximum in the p.m. enthalpy, $-\partial H/\partial x$, in both cycling directions. The
148 maximum is more pronounced in the delithiation direction than for lithiation. This trend is in agreement

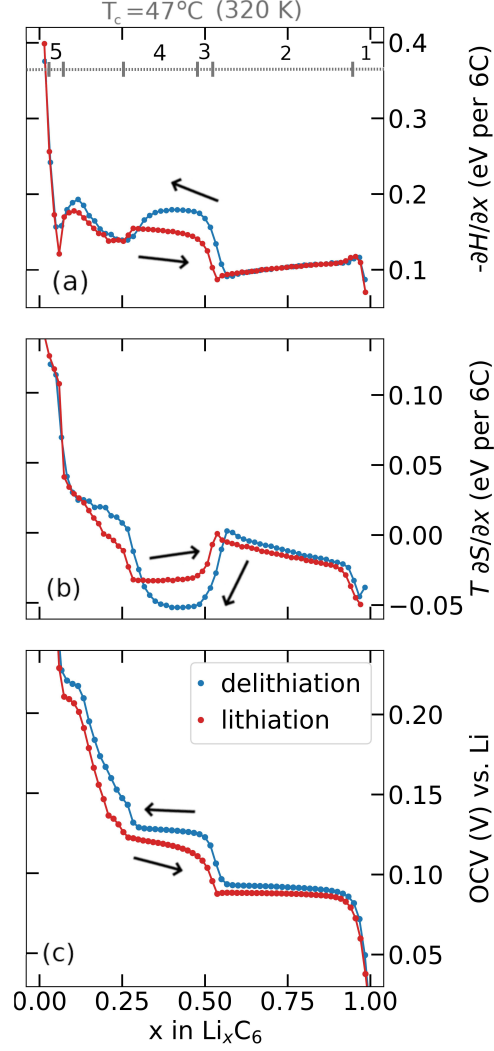


Figure 3: Profiles obtained at central temperature, $T_c = 47^\circ\text{C}$: (a) partial molar (p.m.) enthalpy, (b) p.m. entropy and (c) open circuit voltage obtained during lithiation and delithiation (black arrows indicate direction of cycling), as a function of lithiation degree x in Li_xC_6 . The y-axis T in (b) is the absolute temperature expressed in degrees K, shown at the top of the column. Labelled features 1-5 corresponding to the lithiation profiles are referred to the main text.

149 with the variation in the OCV response, Figure 3c. The p.m. entropy response, Figure 3b shows the opposite
 150 trend in this interval. The difference between the measured OCV in each cycling direction arises mostly from
 151 the p.m. enthalpy term, with partial cancellation due to the $T\partial S/\partial x$ term. The net hysteresis in the OCV
 152 resulting from the enthalpy and entropy terms is approximately 10 mV, in agreement with the values shown
 153 in Figure 3c.

154 2.3 Low temperature ground states from DFT

155 Figure 4a shows the computed formation energies (E_f) of all sampled configurations as a function of Li
 156 content. E_f was determined by equation 10. To be consistent with the derived experimental quantities,

157 normalised in eV per formula unit, the E_f values are likewise normalised by $6N_C$, where N_C is the number
 158 of carbon atoms in the unit cell. The energy landscape within the AA stacking host is shown in blue, the
 159 AABB host in red, and the AB host in pink. Thermodynamic ground-states within each host are connected
 160 by lines, giving convex hulls for each host. The overall thermodynamic ground-states result from a convex
 161 hull construction over all data points (not shown). We find several low energy orderings within the the
 AABB and AA hosts that compete for overall thermodynamic stability.

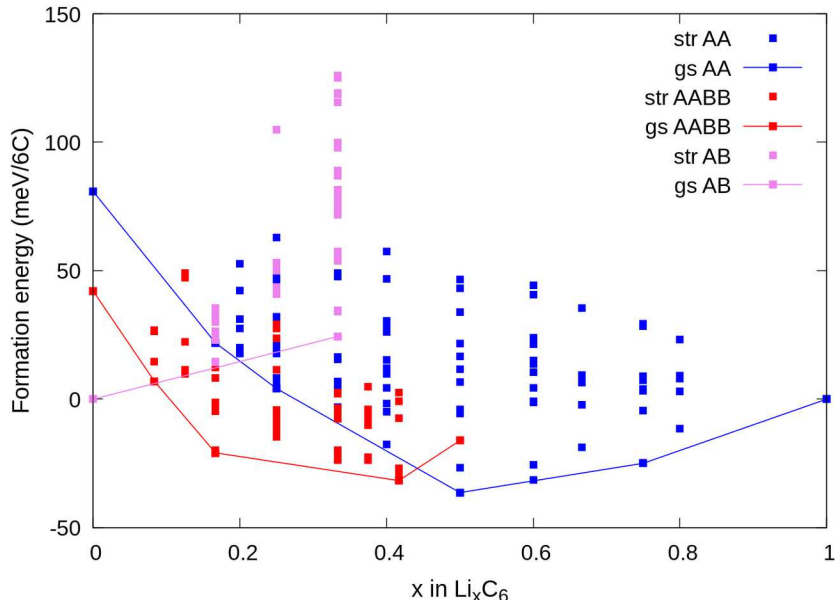


Figure 4: DFT calculations of ground state Li-graphite structures. Convex hull showing the formation energies (units meV/6C) of ground states from: *blue line*: stages I and stage II with AA carbon stacking; *red line*: dilute stage II with AABB carbon stacking; *pink line*: other dilute stage compounds with AB stacking. “str”: structures sampled by cluster expansion; “gs”: ground state structures.

162

163 The results are consistent with the experimentally observed stacking sequences as a function of x . The
 164 AA-stacked stages I and II are favoured for $x \geq 0.5$; AABB stacking (dilute Stage II) is favoured over AB or
 165 AA stackings at intermediate x , and AB-stacked graphite is the ground-state for $x \rightarrow 0$. It is also possible to
 166 draw a common tangent between the respective convex hulls for AABB and AA stackings (indicated by the
 167 red dashed line in Figure 5a) reflecting the two-phase coexistence of dilute Stage II and Stage II compounds.
 168 Finally, a similar common tangent construction would be possible between AB and AABB stackings that
 169 does not reflect experimentally confirmed two-phase equilibria at low concentrations, which we attribute to
 170 us not considering the Stage III and Stage IV compounds.

171 2.4 Thermodynamics of carbon stacking and cycle direction

172 Our experimental results have shown that the p.m. enthalpy depends on cycling direction in the range
 173 $0.25 < x < 0.5$, which we propose is due to graphite retaining AAAA stacking during delithiation well below
 174 $x = 0.5$ and only transitioning to the thermodynamically favoured AABB stacking (and/or AB) at much
 175 lower Li content. In the lithiation direction, on the other hand, the structure closely follows the AABB
 176 ground state configuration for approximately $0.17 < x < 0.5$. Stacking transitions then occur during the two
 177 phase coexistence interval between the AABB and AAAA hosts. For $x \geq 0.5$, we expect the same AAAA
 178 carbon stacking in both cycling directions for $0.5 \leq x \leq 1$.

179 The scheme is visualised in Figure 5a. This shows the computed convex hulls for the AAAA and AABB-
 180 stacked systems. The dashed lines indicate the slope of the formation energy with respect to the Li concen-
 181 tration, x in the concentration range of interest. This slope is a chemical potential for lithium intercalation,
 182 μ , by equation 3. However, because DFT calculations probe the ground state energy, the presented formation
 energies exclude partial molar entropy and thus are more precisely related to the partial molar enthalpy.

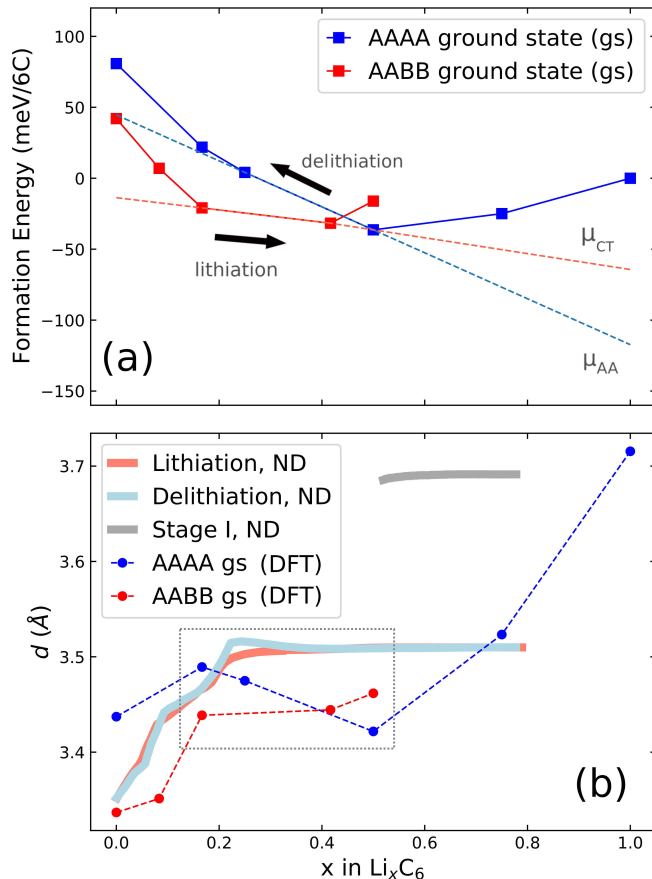


Figure 5: (a) Illustration of possible cycling pathways along the ground state (gs) free energy curves presented in Figure 4a. The slope of the red dashed line designates a chemical potential, μ_{CT} , which we propose is followed during lithiation. During delithiation, the AAAA-stacked structure persists as lithium is extracted from the host lattice, corresponding to chemical potential μ_{AA} . (b) Results obtained from neutron diffraction (ND) data. The average interlayer carbon distance, d , is shown as a function of lithium concentration x . Reprinted (adapted) with permission from Fig. 1 of ref. [12]. Copyright 2020 American Chemical Society. d values obtained from the AAAA and AABB-stacked DFT ground states from the present work are overlaid for comparison.

183

184 Regardless, the scheme in Figure 5a suggests a more negative chemical potential if the structure follows an
 185 AAAA-stacked configuration during delithiation for $x < 0.5$ than given by the AABB to AAAA two-phase
 186 coexistence interval expected during lithiation. By equation 2, this translates into a more negative partial
 187 molar enthalpy, and therefore more positive OCV, during delithiation than during lithiation, which is exactly
 188 the trend observed experimentally as compared in Table 2, although the *ab-initio* results predict a slightly
 189 stronger effect than experimentally observed.

Table 2: Comparison of experimental values obtained from partial molar enthalpy measurements with chemical potentials evaluated from DFT calculations, in each cycling direction, at $x = 0.41$. The difference in values between lithiation and delithiation is compared.

Transition at $x < 0.5$	μ (DFT) (eV per 6C)	$\partial H/\partial x$ (experiment) (eV per 6C)
Lithiation (l)	-0.056	-0.150
Delithiation (d)	-0.162	-0.179
Difference (l-d)	0.106	0.029

190 The quantitative enthalpy difference between theory and experiment could be because of (i) systematic errors
 191 from the van-der-Waals correction to the exchange-correlation functional used in the DFT calculations and
 192 (ii) to the fact that we are comparing 0 K calculations to 320 K experiments. The experimental value could
 193 also be different due to deviations from ideal carbon stacking (turbostratic disorder), additional effects from
 194 interplanar Li sites, as analysed quantitatively later, or other types of structural defects.

195 The scheme is consistent with experimentally determined neutron diffraction (ND) studies of the average
 196 interlayer carbon spacing, d [12, 8, 9]. Those studies suggest asymmetry in the formation of Stage IID during
 197 lithiation and delithiation. We compare the results of in-operando neutron diffraction from the recent paper
 198 of Didier et al. [12] to the average interlayer carbon spacing, d , of the ground state structures calculated by
 199 DFT. d values were obtained by visualising the ground state unit cells within VESTA [37] and determining
 200 the most intense peak from simulated powder XRD patterns. The resultant d values are overlaid with the
 201 neutron diffraction data from ref. [12] in Figure 5b. The region of interest is highlighted in the dashed grey
 202 box.

203 Results in the Stage I region, and also for stages greater than I, suggest that DFT systematically underes-
 204 timates the interlayer carbon spacing compared with experiment. Systematic differences between predicted
 205 and experimental d values were found previously from DFT [38], but it is nonetheless instructive to compare
 206 the trends between theory and experiment. In the interval $0.17 < x < 0.41$, there is a slight gradual increase
 207 in d predicted as a function of x , while d is predicted to remain almost constant over the same concentration
 208 range in the AABB host. The same decrease of d is seen in the experimental profiles obtained from delithi-
 209 ation but absent in the opposite direction. We take this as further evidence that the lattices remains in an
 210 AAAA-stacked configuration as x decreases below 0.5 during delithiation.

211 2.5 Energetic barriers for stacking shifts

212 The existence of meta-stable AAAA-stacked carbon during delithiation would suggest activation barriers for
 213 transitioning between AABB and AAAA stackings at intermediate Li concentrations. Otherwise, AAAA
 214 configurations would not be meta-stable and spontaneously convert to AABB as soon as x is small enough
 215 to thermodynamically favour AABB stacking. Based on the ground state structures found from the cluster
 216 expansion, activation energies for transitions between different carbon stackings were evaluated through the
 217 climbing image nudged elastic band (NEB) method [39, 40]. In the NEB calculations, a motif in the unit
 218 cell was translated along a path, as represented in Figure 6.

219 We found no relevant activation energy barriers for carbon layers shifting between AABB and AAAA stacking
 220 or AB and AA stacking. A result is shown at a select concentration of $x = 0.5$ in Figure 6b. A full
 221 analysis over a range of x values can be found in Figure S2 and S3 in the Supplementary Information.
 222 There always exists a smooth, monotonous path connecting the ground-state stacking to possible alternative
 223 carbon stackings without a transition state. Therefore, energetic barriers to translate between different
 224 carbon stackings alone do not explain the hysteresis effect.

225 Figure 6b indicates that $A\alpha AA\alpha A$ stacking is energetically favourable at $x = 0.5$, consistent with the ground
 226 states from the cluster expansion (Figure 4). These ground states exclude thermal excitations, which could
 227 transfer a small fraction of lithium to the interplanar sites. Indeed, our cluster expansion within the AAAA

228 host suggests interplanar Li is energetically competitive within this stacking at $x = 0.17$ (points **2** and **3** in
 229 Figure 6c-d. Figure 6d, structure **3** shows that the AAAA ground state involves Li occupying interplanar
 230 sites, while structure **1**, the AABB ground state and the overall lowest energy structure, shows Li occupying
 231 only every alternate plane, because of the unfavourable Li site environment between AB sheets.

232 Figure 6c shows NEB energy profiles obtained at $x = 0.17$, considering translations of the highlighted motifs
 in Figure 6d along the indicated path.

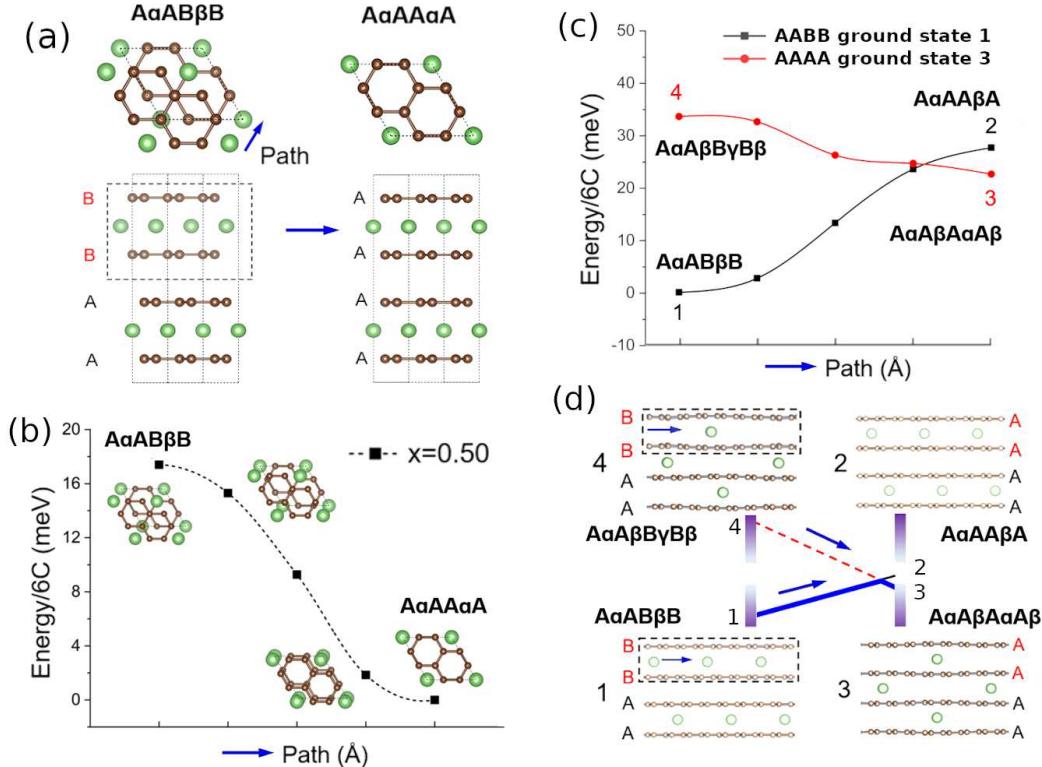


Figure 6: Nudged elastic band (NEB) calculations of layer translations. (a) Top down and side views representing the transition from AABβB to AαAAαA stacking in the host lattice. The entire highlighted motif is translated along the indicated direction. (b) Energy profiles of transitions between AABβB to AαAAαA host lattice stacking obtained at $x = 0.5$ (c) Energy profiles of stacking transitions at $x = 0.17$ using lattices based on the AABβB ground state (denoted as 1) and AαAAαA ground state (denoted as 3), respectively. (d) Side views representing the carbon and lithium orderings at the two end points of the path. In (c) and (d) the notation indicates the lithium and carbon stackings at the two ends of the NEB path.

233

234 The absence of lithium in the interlayer of structure **1** leads to a different qualitative energy change when the
 235 carbon layers transition from AABβB to AαAAαA stacking (path **1** → **2** - uphill), than when the layers transition
 236 with lithium present in the interlayer (**4** → **3** - downhill). The computed energetic difference between **3** and
 237 **2**, the two different lithium arrangements within AAAA stacking, is very small (approximately 5 meV/6C)
 238 and so also is the average interlayer carbon distance, d (**3**: $d = 3.46 \text{ \AA}$, **2**: $d = 3.49 \text{ \AA}$).

239 Plausibly, the presence of interlayer Li sites in AAAA stackings is an important factor determining the di-
 240 rectional dependence of the layer transitions and, therefore, the hysteresis observed in OCV below $x = 0.5$.
 241 AAAA stackings could be stabilised by residual interlayer Li that is more likely to be present during delithi-
 242 ation than during lithiation, which could be a contributing factor to the observed hysteresis at intermediate

243 concentrations $x < 0.5$ even without classical activation barriers for carbon layer shifts or considering possible
 244 barriers from overcoming interface energies.

245 In support of these statements, the proportion of these interlayer Li sites is assessed quantitatively in the
 246 next section.

247 2.6 Interplanar site occupation

248 We performed further analysis the experimental entropy profiles from section 4.3. The configurational
 249 entropy, S_{config} , contains additional information regarding the interplanar Li site occupation. S_{config} can be
 250 extracted from the profiles shown in Figure 3b using the methods described in section 4.5.

251 Results for S_{config} as a function of x are shown in Figure 7a, which was obtained by applying equation 9 to the
 252 experimental result for $\partial S/\partial x$ obtained at $T = 320$ K, i.e. Figure 3b. The total capacity of the Li/graphite
 253 cells was consistently found to be below the theoretical one of 372 mAh/g. Therefore, we multiplied x by
 254 a correction factor so that value of S_{config} at maximum lithiation matched the dashed solid solution line
 corresponding to a Stage I solid solution.

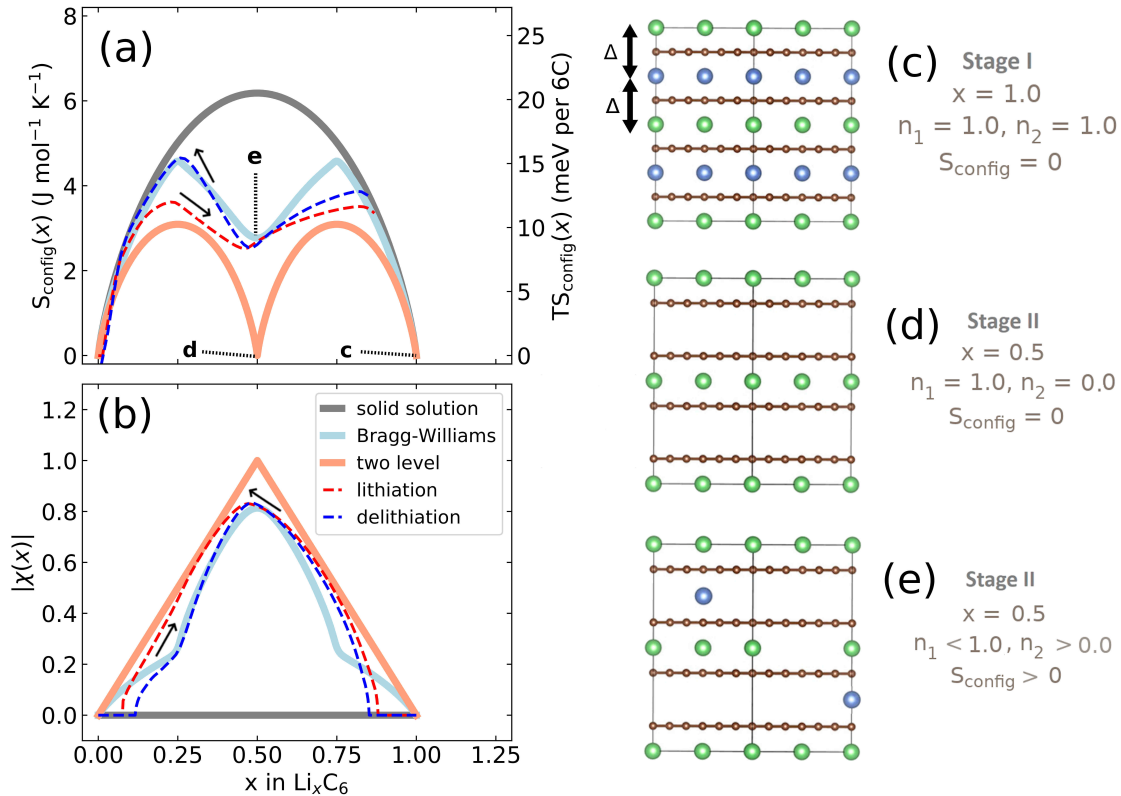


Figure 7: (a) Configurational entropy obtained at central temperature $T = 320$ K: *dark grey solid line*: ideal solid solution; *light blue solid line*: Bragg-Williams solution with interplanar mean field Li-Li repulsion of 75 meV; *salmon solid line*: sequential two level solid solution; *red dashed line*: experimental lithiation; *blue dashed line*: experimental delithiation. (b) Order parameter $|\chi|$, as described in the main text, labelled as in (a). In (a), select points (c-e) are indicated and schematic representations of the lattice occupations of Li in levels n_1 (green balls) and n_2 (blue balls) are shown on the right.

255

256 The Li occupation in each alternate layer can be considered in sublattices n_1 and n_2 for a given x , with
 257 representative examples shown in Figure 7c-e, such that $x = (n_1 + n_2)/2$. Solid lines in Figure 7a-b indicate
 258 three hypothetical cases. The salmon pink line denotes sequential filling of Li into two well-separated energy
 259 levels. This case, with $S_{\text{config}}(x)$ described in equations S5 and S6, results in each alternate plane between
 260 the carbon sheets being filled randomly with Li up to $x = 0.5$; only then the next layer fills above $x = 0.5$.
 261 The dark grey line shows the result for an ideal solid solution, equation S4 if Li were to fill all available sites
 262 at random, i.e. $n_1 = n_2$ for all x . The blue solid line is the solution to a Bragg-Williams model [31] assuming
 263 only nearest neighbour repulsive pairwise lithium interactions between planes of $\Delta = 75$ meV and no in-
 264 plane interactions. The model produces a behaviour in $S_{\text{config}}(x)$ intermediate between the solid solution
 265 and sequential two level filling. At $x = 1$, there is a net repulsion on each Li atom of 2Δ , as represented in
 266 Figure 7c. At $x = 0.5$, this model results in one of the sublattices being preferentially filled, as represented
 267 schematically in Figure 7e. In contrast, a perfect Stage II structure as predicted by sequential two level
 268 filling (Figure 7d) would result in $S_{\text{config}}(0.5) = 0$.

269 Experimental results for lithiation and delithiation, shown as dashed lines, feature two peaks, with a local
 270 minimum centred at $x \approx 0.5$. Both curves show a very similar value of $TS_{\text{config}} \approx 10$ meV per 6C at $T = 320$
 271 K, indicating nearly the same lattice configuration at $x = 0.5$.

272 It is beneficial to construct a “staging order parameter”, $\chi(x) = n_1 - n_2$, to quantify the interlayer Li disorder
 273 [41], which is plotted in Figure 7b. Formally, $\chi(x)$ takes values between -1 and +1 but only the absolute
 274 value is meaningful here. If $|\chi(x)| = 1$, then only one layer is filled with Li, representing maximal staging
 275 order. If $\chi(x) = 0$, both layers are occupied with equal probability, disorder is maximal and no staging
 276 is observed. The required occupations of interplanar sites, n_1 and n_2 were obtained from $S_{\text{config}}(x)$, using
 277 equation S7 and applying a numerical procedure detailed in the Supplementary Information.

278 As suggested by the previous results, the trend in order parameter $|\chi(x)|$ is very similar between lithiation and
 279 delithiation for $x \geq 0.5$. At $x = 0.5$ both curves show nearly identical order parameters to the Bragg-Williams
 280 solution of $|\chi(x)| \approx 0.8$. However, there is a pronounced difference in the trend in $|\chi(x)|$ values for $x < 0.5$.
 281 The $|\chi(x)|$ value for delithiation is always greater than the value obtained during lithiation, indicating
 282 that greater configurational order is obtained during lithiation. In fact the experimental delithiation result
 283 closely resembles the Bragg-Williams model, while $|\chi(x)|$ values obtained for lithiation for $x < 0.5$ are only
 284 marginally higher than expected for sequential two level filling.

285 The staging order parameter trends for $x < 0.5$ are consistent with the carbon layer transitions and energetic
 286 trends predicted from DFT. During lithiation only half of the layers are filled with lithium in an AABB-
 287 stacked configuration, consistent with two level filling. The energy level difference can be attributed to the
 288 different Li environment between AA and AB sheets. During delithiation, alternate layers are preferentially
 289 emptied by Li due to repulsive interactions in an AAAA-stacked host, but the Li repulsion is insufficient
 290 to prevent some Li staging disorder, which we propose delays the transition to AABB-stacking. This result
 291 provides further support for the statement from DFT regarding the importance of interplanar sites to the
 292 observed hysteresis effect. It additionally provides insight into the origins of the hysteresis in OCV arising
 293 from the partial molar entropy term.

294 3 Discussion

295 A residual hysteresis is observed in the measured open circuit voltage (OCV) during lithiation and delithi-
 296 ation in graphite. The hysteresis is not reduced even at temperatures $T > 50^\circ\text{C}$. Energetic and entropic
 297 components to the hysteresis were measured. Energetic differences and volume changes from *First Principles*
 298 calculations suggest the system remains in metastable AAAA carbon stacking configurations during delithi-
 299 ation. More interlayer Li disorder during delithiation was determined from measurements, as expected for
 300 Li in AAAA-stacked configurations. No relevant energetic barriers for transitioning between formal ground
 301 state stages were found from DFT. Instead, the interlayer Li sites in Stage II configurations contribute to the

302 hysteresis effect. In combination with the enthalpy difference in each cycling direction, this entropy difference
303 results in a net higher OCV during delithiation. Increasing the temperature does not cause the lithiation
304 and delithiation OCV curves to converge to the same values, since a temperature rise would increase the
305 proportion of occupied sites in the interlayer.

306 The work has implications for control of Li-ion batteries. The open circuit voltage is often considered
307 equivalent to the equilibrium potential at each state of charge, i.e. lithiation fraction in graphite. However,
308 the present results reveal that the cycling direction must also be taken into account under any practical
309 temperature or relaxation time. Models of the OCV used to determine the state of charge in battery
310 management systems (BMS) should take history dependence into account. Due to differences in the d -
311 spacing with cycle direction, in-situ pressure or stress measurements might be beneficial to augment BMS
312 models [29, 42].

313 The entropy behaviour dependent on cycling direction of other materials that are known to show hysteresis
314 should also be explored. As an example, lithium iron phosphate (LFP) particles have shown greater spatial
315 heterogeneity during delithiation than during lithiation [43]. The strategies are also relevant to understanding
316 stacking sequence related changes in layered Li and Na-ion intercalation hosts due to lattice invariant shear
317 [44, 45].

318 4 Methods

319 4.1 Electrode and cell preparation

320 Carbon working electrodes were prepared by a mixture of graphite powder (particle size $< 20\mu\text{m}$, synthetic,
321 Sigma-Aldrich), Super P carbon and polyvinylidene fluoride (PVDF) in N-methyl-2-pyrrolidone (NMP) in a
322 mass ratio of 93:5:2, respectively. The slurry was then cast onto copper foil using a doctor blade, dried and
323 calendared to approximately 80-90 μm thickness to make the working electrode.

324 Stainless steel CR2032 coin cells were used for all measurements. Cells were prepared in an Argon-filled
325 glovebox ($[\text{H}_2\text{O}] < 0.1 \text{ ppm}$, $[\text{O}_2] < 0.1 \text{ ppm}$) with Celgard separator and a 1 M LiPF_6 in a 1:1 wt/wt
326 mixture of ethyl carbonate (EC) and dimethyl carbonate (DMC) electrolyte. Working electrodes of 12 mm
327 diameter were punched out the film using a disc cutter. An oversized 16mm Li foil was used as counter
328 and reference electrode to mitigate effects from inhomogeneous lithiation. All voltages are, consequently,
329 reported with respect to metallic Li.

330 Experimental measurements were performed using aluminium heat exchangers, in direct thermal contact
331 with the coin cells, which were connected to a Julabo F12 refrigerated – heating circulator, allowing direct
332 control over the cell temperatures. This setup enabled more rapid thermal equilibration of the cells than
333 would be possible using a climate chamber. Temperature was monitored by type-J thermocouples in direct
334 contact with the heat exchangers. A Keysight 34972A data acquisition system with multiplexer unit was
335 used for high resolution (22 bit) voltage and temperature measurements, assisting post processing of entropy
336 profile data. Cell current and voltage was controlled by a BaSyTec CTS cycler. A software interface between
337 the data acquisition unit and the battery cycler allowed real time measurement of temperature, current and
338 voltage to the required resolution. Data points were recorded every 1 s. Further detail of the setup can be
339 found in earlier publications [46, 31, 47].

340 All freshly assembled cells were subjected to a formation protocol before use: three full galvanostatic charge-
341 discharge cycles were performed at a rate of 37.2 mA/g (determined from the active material mass of graphite)
342 corresponding to a C/10 rate. These cycles were performed between voltage limits of 0.050 and 1.500 V,
343 at a controlled temperature of 25 °C. Similar procedures have been used elsewhere [31, 48] and are intended
344 to ensure stable solid electrolyte interphase (SEI) formation and representative cycling performance before
345 performing the slower characterisation techniques described in the next sections.

346 4.2 Constant current/constant voltage protocols

347 All continuous galvanostatic, GITT and entropy profiling measurements described subsequently were pre-
 348 ceded by a constant current/constant voltage (dis)charging protocol, designated "CCCV (dis)charge", to
 349 ensure a consistent starting lithiation state for each experiment. A CCCV charge consists of galvanostatic
 350 delithiation at $C/20$ (18.6 mA/g) up to 1.5 V, followed by at least 2 hours of polarisation at 1.5 V. A CCCV
 351 discharge starts with galvanostatic lithiation at $C/25$ (14.88 mA/g) down to 0.005 V, followed by at least 2
 352 hours of polarisation at 0.005 V. The low C-rate here was designed to mitigate the risk of lithium plating so
 353 close to 0 V, while allowing lithiation as close as possible to the ideal LiC_6 structure ($x = 1$).

354 4.3 Determination of thermodynamic profiles

355 Relevant thermodynamic variables are defined here to ensure consistency between experimental and DFT
 356 results in the preceding sections and to ensure those results are compared on equivalent energy and lithium
 357 concentration scales.

358 It is well known that the equilibrium cell voltage, $\phi(x)$ and chemical potential of intercalated Li, $\mu(x)$ are
 359 related as

$$\phi(x) = -\frac{\mu(x) - \mu_{\text{Li}}^{\text{ref}}}{nF}, \quad (1)$$

where $\mu_{\text{Li}}^{\text{ref}}$ is the chemical potential of the metallic Li anode reference, which is defined as zero on our
 reference scale. $n = 1$ is the number of electrons transferred per LiC_6 formula unit, and F is the Faraday
 constant. With a suitable choice of units for all potentials (μ expressed in eV per formula unit), this can be
 written much more simply as

$$\phi(x) = -\mu(x). \quad (2)$$

360 The intercalated Li chemical potential is defined by

$$\mu(x) = \left(\frac{\partial \underline{G}(x)}{\partial N_{\text{Li}}} \right)_{p, T, N_{\text{host}}} = \left(\frac{\partial G(x)}{\partial x} \right)_{p, T, N_{\text{host}}}, \quad (3)$$

361 where \underline{G} = the absolute (i.e. extensive) Gibbs free energy, p = pressure, T = the absolute temperature, N_{host}
 362 and N_{Li} are respectively the number of carbon and lithium atoms in the system. As there is one Li atom per
 363 LiC_6 formula unit, with x expressing the fraction of lithium in Li_xC_6 ($0 \leq x \leq 1$), i.e. $x = N_{\text{Li}}/(6N_{\text{host}})$.
 364 G is the Gibbs free energy per formula unit of 6C . The subscripts p , T and N_{host} will be implicitly assumed
 365 constant from now on and dropped for simplicity.

Likewise it is well known that

$$\frac{\partial G(x)}{\partial x} = \frac{\partial H(x)}{\partial x} - T \frac{\partial S(x)}{\partial x}, \quad (4)$$

366 where $H(x)$ and $S(x)$ are the enthalpy and entropy, respectively, per formula unit of host material.

367 Assuming that the OCV, E_{OCV} , measured at the end of the relaxation period for each x value corresponds
 368 to $\phi(x)$, we can use equations 2, 3 and 4 to get $\partial G/\partial x = -E_{\text{OCV}}$. Then, taking the derivative of the OCV
 369 with respect to T and using the chain rule, we obtain

$$\frac{\partial E_{\text{OCV}}(x)}{\partial T} = \frac{\partial S(x)}{\partial x} - \frac{\partial}{\partial x} \left[T \left(\frac{\partial S(x)}{\partial T} \right)_{p, N_{\text{host}}} - \left(\frac{\partial H(x)}{\partial T} \right)_{p, N_{\text{host}}} \right]. \quad (5)$$

370 However,

$$T \left(\frac{\partial S(x)}{\partial T} \right)_{p, N_{host}} = \left(\frac{\partial H(x)}{\partial T} \right)_{p, N_{host}} = C_p, \quad (6)$$

where C_p is the specific heat capacity at constant pressure. Hence we can simplify equation 5 as

$$\frac{\partial S(x)}{\partial x} = \frac{\partial E_{OCV}(x)}{\partial T} \quad (7)$$

and so

$$\frac{\partial H(x)}{\partial x} = T \frac{\partial E_{OCV}(x)}{\partial T} - E_{OCV}(x). \quad (8)$$

Due to the choice of units of eV per formula unit for the potentials $H(x)$ and $TS(x)$, i.e. as in the conversion between equations 1 and 2, the usual factors of F have been omitted. All of the terms in equations 7 and 8 are measurable using methods described in section 4.4.

4.4 Entropy profiling and open circuit voltage measurement

We used similar methods as in our previous work to obtain entropy profiles under lithiation conditions [46, 31, 47]. The method is akin to GITT, comprising alternating steps under galvanostatic control followed by relaxation under open circuit conditions, but in addition the temperature is varied during the relaxation period and entropy is calculated from the gradient of OCV with temperature. Measurements comprised iterative steps of galvanostatic (dis)charge at C/25 followed by a total of 80 minutes of relaxation time.

All entropy profiling measurements were preceded by a constant current/constant voltage (dis)charging protocol, designated "CCCV (dis)charge", to ensure a consistent starting lithiation state for each experiment. A CCCV charge consisted of galvanostatic delithiation at C/20 (18.6 mA/g) up to 1.5 V, followed by at least 2 hours of polarisation at 1.5 V. A CCCV discharge started with galvanostatic lithiation at C/25 (14.88 mA/g) down to 0.005 V, followed by at least 2 hours of polarisation at 0.005 V. The low C-rate here was designed to mitigate the risk of lithium plating so close to 0 V, while allowing lithiation as close as possible to the ideal LiC_6 structure ($x = 1$).

Entropy profiling in lithiation mode was performed in an iterative procedure, where the current and temperature were changed dynamically as outlined in Table 3. The central temperature, T_c was varied as indicated in the results section of the main paper. Entropy measurements comprising iterative steps of galvanostatic discharge were initiated by performing a "CCCV charge" step at $T = T_c + 3^\circ\text{C}$. Each iteration was repeated until the cell voltage was less than 0.005 V, mirroring the cutoff voltage of the CCCV discharge procedure. State of charge, x , was obtained from normalising the change of capacity from each galvanostatic step in Table 3 to the total change of capacity obtained during the entire experiment.

Table 3: Conditions applied during each iteration of the entropy profiling experiments. An example temperature profile at $T_c = 25^\circ\text{C}$ is illustrated for clarity in the right hand column.

Step	Time (min)	Temperature T ($^\circ\text{C}$)	Applied T at $T_c = 25^\circ\text{C}$
Discharge (C/25)	20	$T_c + 3$	28
OCV relaxation	20	$T_c + 3$	28
Temperature step T_1 at OC	20	T_c	25
Temperature step T_2 at OC	20	$T_c - 3$	22
Temperature step T_3 at OC	20	$T_c + 3$	28

We also performed a set of measurements where profiles were initiated from a "CCCV discharge" at $T = T_c + 3^\circ\text{C}$, and the graphite electrode was delithiated stepwise at C/25. These experiments were cut off once

397 the cell voltage reached a value greater than 1.5 V. The temperature program in Table 3 was also used here,
398 except that step 1 was a charge rather than a discharge.

399 The target variable from the temperature program shown in Table 3 is the slope of the open circuit voltage
400 (E_{OCV}) with respect to temperature, i.e. ($\partial E_{\text{OCV}}/\partial T$), at constant x , as shown in section 4.3. We applied the
401 OCV background subtraction methods developed in our previous work [46] to subtract the time-dependent
402 voltage drift and avoid excessive measurement times for each x value.

403 4.5 Extracting configurational entropy

404 The experimental p.m. entropy profiles from section 2.2 can be further analysed to obtain the configurational
405 entropy, S_{config} , of lithium in graphite. The total entropy naturally is a sum of configurational, vibrational
406 and electronic components [32, 49, 33].

407 The electronic entropy contribution [32, 49, 33], which should not vary much with x , can be neglected.
408 However, Reynier et al. showed the vibrational entropy, S_{vib} , of Li in graphite to be significant [32]. Previous
409 experimental [50] and theoretical [38] investigations also showed differences in the vibrational modes of
410 Li in the different Li-graphite stages. Fortunately, S_{vib} can be estimated by approximating the phonon
411 spectrum with a single Debye temperature for each vibrational mode [32, 51, 52] (c.f. the Supplementary
412 Information for details). By taking the raw partial molar entropy data as shown in Figure 3e and subtracting
413 the vibrational entropy component obtained for each x value, the partial molar configurational entropy,
414 $\partial S_{\text{config}}/\partial x$, can be obtained, as shown in Figure S4. Then by integration

$$\int_{x'=0}^{x'=x} \left(\frac{\partial S_{\text{config}}(x')}{\partial x'} \right) dx' = S_{\text{config}}(x) \approx S(x) - S_{\text{vib}}(x), \quad (9)$$

415 we obtain $S_{\text{config}}(x)$. The integration constant is $S_{\text{config}}(x=0) = 0$, because there can be no Li disorder in
416 pure graphite.

417 4.6 Computational methods

418 Spin-polarized Density-Functional-Theory (DFT) calculations were performed using the Vienna Ab-Initio
419 Simulation Package (VASP) [53, 54, 55, 56]. The Perdew-Burke-Ernzerhof (PBE) functional within the
420 generalized gradient approximation has been used throughout [57]. The projector-augmented wave method
421 was used to represent the core electrons [58]. The valence electronic states were expanded in plane-wave basis
422 sets with cutoff energies of 450 eV. Periodic boundary conditions were applied in all three dimensions. The
423 force convergence criterion in structural optimization was set to be 0.03 eV/Å. A k-mesh of (12×12×7) was
424 used for AαB and AαA stacked hosts and a (11×11×3) k-mesh for AαABβB stacked hosts. The DFT-D2
425 method was employed to describe Van der Waals interactions [59].

426 The cluster expansion method, implemented within the Alloy Theoretic Automated Toolkit (ATAT) [60, 61],
427 was used to efficiently sample low energy Li configurations within the respective carbon stackings. The energy
428 of a configuration was calculated within Density-Functional-Theory using the Vienna Ab-Initio Software
429 Package (VASP). Details of the input parameters and exchange-correlation functional are in section 4.6. In
430 lithiated graphite, the stackings of AαBα, AαABβB and AαAα were used as the parent lattices to sample
431 configurations with prototype structures shown in Figure S1. The cluster expansions of AA, AABB and AB
432 stackings were well converged after sampling 87, 126 and 58 different Li ordering configurations, respectively.
433 For each cluster expansion, the configurational degrees of freedom included only Li sites, i.e. we froze carbon
434 stacking degrees of freedom (while allowing the lattice constant to relax) and confined calculations to a small
435 number of experimentally confirmed stackings, representing the Li-graphite stages shown in Figure 1.

Consistent reference energies across hosts, AB-stacked carbon ($x = 0$) and AA-stacked LiC_6 ($x = 1$), were used for all cluster expansions. The formation energy, E_f was thus determined by

$$E_f = E(\text{Li}_x\text{C}_6) - (1 - x)E(\text{C}_6) - xE(\text{LiC}_6), \quad (10)$$

436 where $E(\text{Li}_x\text{C}_6)$, $E(\text{C}_6)$ and $E(\text{LiC}_6)$ are the energies of the sampled configuration, AB-stacked graphite
437 ($x = 0$) and AA-stacked LiC_6 ($x = 1$), respectively.

438 The climbing-image nudged elastic band (NEB) method was used to search for the transition states (TSs)
439 of the structure transformation, with three images considered between the initial and final state [39, 40].

440 Data availability

441 The experimental and DFT data are available from the lead author (m.mercer1@lancaster.ac.uk) on request.

442 Code availability

443 The code used to determine the entropy coefficients from temperature controlled GITT experiments,
444 and to post-process the entropy data to obtain order parameters is available from the lead author
445 (m.mercer1@lancaster.ac.uk) on request.

446 Acknowledgments

447 MPM, CP, HEH and DK thank the Faraday Institution (faraday.ac.uk; EP/S003053/1), grant number
448 FIRG003, for funding. CS thanks the EPSRC for PhD funding. We thank Richard Fields from University of
449 Manchester Graphene Engineering Innovation Centre for providing the coatings used in the electrochemical
450 measurements, and Miriam Ferrer-Huerta from the Department of Chemistry at Lancaster University for
451 assistance in the experimental set up. Special thanks to David Hovey from the University of Oxford for
452 discussions on the use of the OCV in battery control models.

453 Author contributions

454 All authors contributed to the preparation, editing and review of the manuscript and proof-read and approved
455 the submission. MPM, HEH and DK conceived the study. MPM performed the experimental character-
456 isation and analysis, including the entropy calculations. CP performed the DFT and NEB calculations.
457 CS assembled the electrochemical cells. HEH contributed to the experimental design. DK advised on the
458 theoretical methodologies.

459 Competing interests

460 The authors declare no competing interests.

461 References

462 [1] Dahn, J. R. Phase diagram of Li_xC_6 . *Physical Review B* **44**, 9170–9177 (1991). URL <https://link.aps.org/doi/10.1103/PhysRevB.44.9170>.
463

- 464 [2] Ohzuku, T. Formation of Lithium-Graphite Intercalation Compounds in Nonaqueous Electrolytes
465 and Their Application as a Negative Electrode for a Lithium Ion (Shuttlecock) Cell. *Journal of The*
466 *Electrochemical Society* **140**, 2490 (1993). URL [https://iopscience.iop.org/article/10.1149/1.](https://iopscience.iop.org/article/10.1149/1.2220849)
467 [2220849](https://iopscience.iop.org/article/10.1149/1.2220849).
- 468 [3] Konar, S., Häusserman, U. & Svensson, G. Intercalation compounds from LiH and graphite: Relative
469 stability of metastable stages and thermodynamic stability of dilute stage Id. *Chemistry of Materials*
470 **27**, 2566–2575 (2015). URL <https://pubs.acs.org/doi/abs/10.1021/acs.chemmater.5b00235>.
- 471 [4] Guerard, D. & Herold, A. Intercalation of lithium into graphite and other carbons. *Carbon* **13**, 337 –
472 345 (1975). URL <http://www.sciencedirect.com/science/article/pii/0008622375900408>.
- 473 [5] Woo, K. C. *et al.* Effect of In-Plane Density on the Structural and Elastic Properties of Graphite
474 Intercalation Compounds. *Phys. Rev. Lett.* **50**, 182–185 (1983). URL [https://link.aps.org/doi/10.](https://link.aps.org/doi/10.1103/PhysRevLett.50.182)
475 [1103/PhysRevLett.50.182](https://link.aps.org/doi/10.1103/PhysRevLett.50.182).
- 476 [6] He, H., Huang, C., Luo, C.-W., Liu, J.-J. & Chao, Z.-S. Dynamic study of Li intercalation into
477 graphite by in situ high energy synchrotron XRD. *Electrochimica Acta* **92**, 148–152 (2013). URL
478 <https://doi.org/10.1016/j.electacta.2012.12.135>.
- 479 [7] Yazami, R. & Reynier, Y. Thermodynamics and crystal structure anomalies in lithium-intercalated
480 graphite. *Journal of Power Sources* **153**, 312 – 318 (2006). URL [http://www.sciencedirect.com/](http://www.sciencedirect.com/science/article/pii/S0378775305007500)
481 [science/article/pii/S0378775305007500](http://www.sciencedirect.com/science/article/pii/S0378775305007500).
- 482 [8] Senyshyn, A. *et al.* Lithium Intercalation into Graphitic Carbons Revisited: Experimental Evidence
483 for Twisted Bilayer Behavior. *Journal of the Electrochemical Society* **160**, A3198–A3205 (2013). URL
484 <http://jes.ecsdl.org/cgi/doi/10.1149/2.031305jes>.
- 485 [9] Taminato, S. *et al.* Real-time observations of lithium battery reactions - Operando neutron diffraction
486 analysis during practical operation. *Scientific Reports* **6**, 28843 (2016). URL [https://www.nature.](https://www.nature.com/articles/srep28843)
487 [com/articles/srep28843](https://www.nature.com/articles/srep28843).
- 488 [10] Cañas, N. A. *et al.* Operando X-ray diffraction during battery cycling at elevated temperatures: A
489 quantitative analysis of lithium-graphite intercalation compounds. *Carbon* **116**, 255–263 (2017). URL
490 <http://linkinghub.elsevier.com/retrieve/pii/S0008622317301203>.
- 491 [11] Billaud, D., Henry, F., Lelaurain, M. & Willmann, P. Revisited structures of dense and dilute stage
492 II lithium-graphite intercalation compounds. *Journal of Physics and Chemistry of Solids* **57**, 775–781
493 (1996). URL <https://www.sciencedirect.com/science/article/pii/0022369795003487>.
- 494 [12] Didier, C., Pang, W. K., Guo, Z., Schmid, S. & Peterson, V. K. Phase Evolution and Intermittent Disorder
495 in Electrochemically Lithiated Graphite Determined Using in Operando Neutron Diffraction. *Chem-*
496 *istry of Materials* **32**, 2518–2531 (2020). URL [https://pubs.acs.org/doi/10.1021/acs.chemmater.](https://pubs.acs.org/doi/10.1021/acs.chemmater.9b05145)
497 [9b05145](https://pubs.acs.org/doi/10.1021/acs.chemmater.9b05145).
- 498 [13] Sethuraman, V. A., Hardwick, L. J., Srinivasan, V. & Kostecki, R. Surface structural disordering in
499 graphite upon lithium intercalation/deintercalation. *Journal of Power Sources* **195**, 3655–3660 (2010).
500 URL <http://dx.doi.org/10.1016/j.jpowsour.2009.12.034>. [1108.0846](https://doi.org/10.1016/j.jpowsour.2009.12.034).
- 501 [14] Sole, C., Drewett, N. E. & Hardwick, L. J. In situ Raman study of lithium-ion intercalation into
502 microcrystalline graphite. *Faraday Discussions* **172**, 223–237 (2014). URL [https://pubs.rsc.org/](https://pubs.rsc.org/en/content/articlelanding/2014/fd/c4fd00079j#!divAbstract)
503 [en/content/articlelanding/2014/fd/c4fd00079j#!divAbstract](https://pubs.rsc.org/en/content/articlelanding/2014/fd/c4fd00079j#!divAbstract).
- 504 [15] Trucano, P. & Chen, R. Structure of graphite by neutron diffraction. *Nature* **258**, 136–137 (1975). URL
505 <https://doi.org/10.1038/258136a0>.
- 506 [16] Okamoto, H. The C-Li (Carbon-Lithium) system. *Bulletin of Alloy Phase Diagrams* **10**, 69–72 (1989).
507 URL <https://doi.org/10.1007/BF02882178>.

- 508 [17] Billaud, D. & Henry, F. Structural studies of the stage III lithium-graphite intercalation compound.
509 *Solid State Communications* **124**, 299 – 304 (2002). URL [http://www.sciencedirect.com/science/
510 article/pii/S0038109802004696](http://www.sciencedirect.com/science/article/pii/S0038109802004696).
- 511 [18] Levi, M., Wang, C., Aurbach, D. & Chvoj, Z. Effect of temperature on the kinetics and thermody-
512 namics of electrochemical insertion of Li-ions into a graphite electrode. *Journal of Electroanalytical
513 Chemistry* **562**, 187 – 203 (2004). URL [http://www.sciencedirect.com/science/article/pii/
514 S0022072803005333](http://www.sciencedirect.com/science/article/pii/S0022072803005333).
- 515 [19] Birkel, C. R., Roberts, M. R., McTurk, E., Bruce, P. G. & Howey, D. A. Degradation diagnostics for
516 lithium ion cells. *Journal of Power Sources* **341**, 373 – 386 (2017). URL [http://www.sciencedirect.
517 com/science/article/pii/S0378775316316998](http://www.sciencedirect.com/science/article/pii/S0378775316316998).
- 518 [20] Li, Y. *et al.* Data-driven health estimation and lifetime prediction of lithium-ion batteries: A review.
519 *Renewable and Sustainable Energy Reviews* **113**, 109254 (2019). URL [http://www.sciencedirect.
520 com/science/article/pii/S136403211930454X](http://www.sciencedirect.com/science/article/pii/S136403211930454X).
- 521 [21] Zheng, T., Reimers, J. N. & Dahn, J. R. Effect of turbostratic disorder in graphitic carbon hosts on the
522 intercalation of lithium. *Physical Review B* **51**, 734–741 (1995). URL [https://journals.aps.org/
523 prb/abstract/10.1103/PhysRevB.51.734](https://journals.aps.org/prb/abstract/10.1103/PhysRevB.51.734).
- 524 [22] Allart, D., Montaru, M. & Gualous, H. Model of Lithium Intercalation into Graphite by Potentiometric
525 Analysis with Equilibrium and Entropy Change Curves of Graphite Electrode. *Journal of The Elec-
526 trochemical Society* **165**, A380–A387 (2018). URL [http://jes.ecsdl.org/lookup/doi/10.1149/2.
527 1251802jes](http://jes.ecsdl.org/lookup/doi/10.1149/2.1251802jes).
- 528 [23] Gallagher, K. G., Dees, D. W., Jansen, A. N., Abraham, D. P. & Kang, S.-H. A Volume Aver-
529 aged Approach to the Numerical Modeling of Phase-Transition Intercalation Electrodes Presented for
530 LixC6. *Journal of The Electrochemical Society* **159**, A2029–A2037 (2012). URL [http://jes.ecsdl.
531 org/lookup/doi/10.1149/2.015301jes](http://jes.ecsdl.org/lookup/doi/10.1149/2.015301jes).
- 532 [24] Grimsman, F. *et al.* Hysteresis and current dependence of the graphite anode color in a lithium-ion
533 cell and analysis of lithium plating at the cell edge. *Journal of Energy Storage* **15**, 17 – 22 (2018). URL
534 <http://www.sciencedirect.com/science/article/pii/S2352152X17302268>.
- 535 [25] Assat, G., Glazier, S. L., Delacourt, C. & Tarascon, J.-M. Probing the thermal effects of voltage
536 hysteresis in anionic redox-based lithium-rich cathodes using isothermal calorimetry. *Nature Energy* **4**,
537 647–656 (2019). URL <https://doi.org/10.1038/s41560-019-0410-6>.
- 538 [26] Persson, K., Hinuma, Y., Meng, Y. S., Van der Ven, A. & Ceder, G. Thermodynamic and kinetic
539 properties of the Li-graphite system from first-principles calculations. *Physical Review B* **82**, 125416
540 (2010). URL <papers://08f9d8a1-e8f9-46cb-82ff-aa1834712d5d/Paper/p735>.
- 541 [27] Drüe, M., Seyring, M. & Rettenmayr, M. Phase formation and microstructure in lithium-carbon inter-
542 calation compounds during lithium uptake and release. *Journal of Power Sources* **353**, 58–66 (2017).
543 URL <https://doi.org/10.1016%2Fj.jpowsour.2017.03.152>.
- 544 [28] Funabiki, A. Stage Transformation of Lithium-Graphite Intercalation Compounds Caused by Elec-
545 trochemical Lithium Intercalation. *Journal of The Electrochemical Society* **146**, 2443 (1999). URL
546 <https://doi.org/10.1149%2F1.1391953>.
- 547 [29] Schweidler, S. *et al.* Volume Changes of Graphite Anodes Revisited: A Combined Operando X-ray
548 Diffraction and In Situ Pressure Analysis Study. *The Journal of Physical Chemistry C* **122**, 8829–8835
549 (2018). URL <https://doi.org/10.1021/acs.jpcc.8b01873>. [https://doi.org/10.1021/acs.jpcc.
550 8b01873](https://doi.org/10.1021/acs.jpcc.8b01873).

- 551 [30] Markevich, E., Levi, M. D. & Aurbach, D. New Insight into Studies of the Cycling Performance
552 of Li-Graphite Electrodes. *Journal of The Electrochemical Society* **152**, A778 (2005). URL <https://iopscience.iop.org/article/10.1149/1.1869982/meta>.
553
- 554 [31] Mercer, M. P. *et al.* Transitions of lithium occupation in graphite: A physically informed model in
555 the dilute lithium occupation limit supported by electrochemical and thermodynamic measurements.
556 *Electrochimica Acta* **324**, 134774 (2019). URL <http://www.sciencedirect.com/science/article/pii/S0013468619316457>.
557
- 558 [32] Reynier, Y., Yazami, R. & Fultz, B. The entropy and enthalpy of lithium intercalation into graphite.
559 *Journal of Power Sources* **119-121**, 850–855 (2003). URL <https://www.sciencedirect.com/science/article/pii/S0378775303002854>.
560
- 561 [33] Reynier, Y. F., Yazami, R. & Fultz, B. Thermodynamics of Lithium Intercalation into Graphites
562 and Disordered Carbons. *Journal of The Electrochemical Society* **151**, A422–A426 (2004). URL
563 <http://jes.ecsdl.org/content/151/3/A422.abstract>. <http://jes.ecsdl.org/content/151/3/A422.full.pdf+html>.
564
- 565 [34] Filhol, J. S., Combelles, C., Yazami, R. & Doublet, M. L. Phase diagrams for systems with low free
566 energy variation: A coupled theory/experiments method applied to Li-graphite. *Journal of Physical*
567 *Chemistry C* **112**, 3982–3988 (2008). URL <https://pubs.acs.org/doi/10.1021/jp076597n>.
- 568 [35] Gavilán Arriazu, E. M., López de Mishima, B. A., Oviedo, O. A., Leiva, E. P. M. & Pinto, O. A.
569 Criticality of the phase transition on stage two in a lattice-gas model of a graphite anode in a lithium-
570 ion battery. *Phys. Chem. Chem. Phys.* **19**, 23138–23145 (2017). URL <http://xlink.rsc.org/?DOI=C7CP04253A>.
571
- 572 [36] Thomas, K. E. & Newman, J. Heats of mixing and of entropy in porous insertion electrodes. *Journal of*
573 *Power Sources* **119-121**, 844 – 849 (2003). URL <http://www.sciencedirect.com/science/article/pii/S0378775303002830>.
574
- 575 [37] Momma, K. & Izumi, F. Vesta3 for three-dimensional visualization of crystal, volumetric and morphol-
576 ogy data. *Journal of Applied Crystallography* **44**, 1272–1276 (2011). URL <https://doi.org/10.1107/S0021889811038970>.
577
- 578 [38] Hazrati, E., de Wijs, G. A. & Brocks, G. Li intercalation in graphite: A van der Waals density-functional
579 study. *Phys. Rev. B* **90**, 155448 (2014). URL <https://link.aps.org/doi/10.1103/PhysRevB.90.155448>.
580
- 581 [39] Henkelman, G. & Jónsson, H. Improved tangent estimate in the nudged elastic band method for finding
582 minimum energy paths and saddle points. *The Journal of Chemical Physics* **113**, 9978–9985 (2000).
583 URL <https://doi.org/10.1063%2F1.1323224>.
- 584 [40] Henkelman, G., Uberuaga, B. P. & Jónsson, H. A climbing image nudged elastic band method for
585 finding saddle points and minimum energy paths. *The Journal of Chemical Physics* **113**, 9901–9904
586 (2000). URL <https://doi.org/10.1063%2F1.1329672>.
- 587 [41] Natarajan, A. R., Thomas, J. C., Puchala, B. & Van der Ven, A. Symmetry-adapted order parameters
588 and free energies for solids undergoing order-disorder phase transitions. *Phys. Rev. B* **96**, 134204 (2017).
589 URL <https://link.aps.org/doi/10.1103/PhysRevB.96.134204>.
- 590 [42] Grimsman, F. *et al.* Hysteresis and current dependence of the thickness change of lithium-ion cells with
591 graphite anode. *Journal of Energy Storage* **12**, 132 – 137 (2017). URL <http://www.sciencedirect.com/science/article/pii/S2352152X1730097X>.
592
- 593 [43] Lim, J. *et al.* Origin and hysteresis of lithium compositional spatiodynamics within battery primary
594 particles. *Science* **353**, 566 LP – 571 (2016). URL <http://science.sciencemag.org/content/353/6299/566.abstract>.
595

- 596 [44] Radin, M. D., Alvarado, J., Meng, Y. S. & Van der Ven, A. Role of crystal symmetry in the reversibility
597 of stacking-sequence changes in layered intercalation electrodes. *Nano Letters* **17**, 7789–7795 (2017).
598 URL <https://doi.org/10.1021/acs.nanolett.7b03989>.
- 599 [45] Vinckevićūtė, J., Radin, M. D. & Van der Ven, A. Stacking-sequence changes and na ordering in
600 layered intercalation materials. *Chemistry of Materials* **28**, 8640–8650 (2016). URL [https://doi.org/](https://doi.org/10.1021/acs.chemmater.6b03609)
601 [10.1021/acs.chemmater.6b03609](https://doi.org/10.1021/acs.chemmater.6b03609).
- 602 [46] Osswald, P. J., del Rosario, M., Garche, J., Jossen, A. & Hoster, H. E. Fast and Accurate Measurement
603 of Entropy Profiles of Commercial Lithium-Ion Cells. *Electrochimica Acta* **177**, 270 – 276 (2015). URL
604 <http://www.sciencedirect.com/science/article/pii/S0013468615002376>.
- 605 [47] Schlueter, S., Genieser, R., Richards, D., Hoster, H. E. & Mercer, M. P. Quantifying structure dependent
606 responses in Li-ion cells with excess Li spinel cathodes: matching voltage and entropy profiles through
607 mean field models. *Phys. Chem. Chem. Phys.* **20**, 21417–21429 (2018). URL [http://dx.doi.org/10.](http://dx.doi.org/10.1039/C8CP02989J)
608 [1039/C8CP02989J](http://dx.doi.org/10.1039/C8CP02989J).
- 609 [48] Antonopoulos, B. K., Stock, C., Maglia, F. & Hoster, H. E. Solid electrolyte interphase: Can faster
610 formation at lower potentials yield better performance? *Electrochimica Acta* **269**, 331 – 339 (2018).
611 URL <http://www.sciencedirect.com/science/article/pii/S001346861830495X>.
- 612 [49] Reynier, Y. *et al.* Entropy of Li intercalation in Li_xCoO_2 . *Phys. Rev. B* **70**, 174304 (2004). URL
613 <https://link.aps.org/doi/10.1103/PhysRevB.70.174304>.
- 614 [50] Schirmer, A. *et al.* In-Plane Phonon Density of States of Li-Graphite Intercalation Compounds. *Molec-*
615 *ular Crystals and Liquid Crystals Science and Technology. Section A. Molecular Crystals and Liq-*
616 *uid Crystals* **244**, 299–305 (1994). URL <https://doi.org/10.1080/10587259408050121>. <https://doi.org/10.1080/10587259408050121>.
- 618 [51] Moreh, R., Shnig, N. & Zabel, H. Effective and Debye temperatures of alkali-metal atoms in graphite
619 intercalation compounds. *Phys. Rev. B* **44**, 1311–1317 (1991). URL [https://link.aps.org/doi/10.](https://link.aps.org/doi/10.1103/PhysRevB.44.1311)
620 [1103/PhysRevB.44.1311](https://link.aps.org/doi/10.1103/PhysRevB.44.1311).
- 621 [52] Beg, M. M. & Nielsen, M. Temperature dependence of lattice dynamics of lithium 7. *Phys. Rev. B* **14**,
622 4266–4273 (1976). URL <https://link.aps.org/doi/10.1103/PhysRevB.14.4266>.
- 623 [53] Kresse, G. & Hafner, J. Ab initio molecular dynamics for liquid metals. *Phys. Rev. B* **47**, 558–561
624 (1993). URL <https://link.aps.org/doi/10.1103/PhysRevB.47.558>.
- 625 [54] Kresse, G. & Hafner, J. Ab initio molecular-dynamics simulation of the liquid-metal–amorphous-
626 semiconductor transition in germanium. *Phys. Rev. B* **49**, 14251–14269 (1994). URL <https://link.aps.org/doi/10.1103/PhysRevB.49.14251>.
- 628 [55] Kresse, G. & Furthmüller, J. Efficient iterative schemes for ab initio total-energy calculations using a
629 plane-wave basis set. *Physical Review B* **54**, 11169–11186 (1996). URL [https://doi.org/10.1103/](https://doi.org/10.1103/2Fphysrevb.54.11169)
630 [2Fphysrevb.54.11169](https://doi.org/10.1103/2Fphysrevb.54.11169).
- 631 [56] Kresse, G. & Furthmüller, J. Efficiency of ab-initio total energy calculations for metals and semi-
632 conductors using a plane-wave basis set. *Computational Materials Science* **6**, 15–50 (1996). URL
633 <https://doi.org/10.1016/2F0927-0256%2896%2900008-0>.
- 634 [57] Perdew, J. P., Burke, K. & Ernzerhof, M. Generalized Gradient Approximation Made Simple. *Physical*
635 *Review Letters* **77**, 3865–3868 (1996). URL <https://doi.org/10.1103/2Fphysrevlett.77.3865>.
- 636 [58] Kresse, G. & Joubert, D. From ultrasoft pseudopotentials to the projector augmented-wave method.
637 *Physical Review B* **59**, 1758–1775 (1999). URL <https://doi.org/10.1103/2Fphysrevb.59.1758>.

- 638 [59] Grimme, S. Semiempirical GGA-type density functional constructed with a long-range dispersion cor-
639 rection. *Journal of Computational Chemistry* **27**, 1787–1799 (2006). URL [https://doi.org/10.1002/](https://doi.org/10.1002/2Fjcc.20495)
640 [2Fjcc.20495](https://doi.org/10.1002/2Fjcc.20495).
- 641 [60] van de Walle, A., Asta, M. D. & Ceder, G. The Alloy Theoretic Automated Toolkit: A user
642 guide. *Calphad* **26**, 539–553 (2002). URL [https://www.sciencedirect.com/science/article/pii/](https://www.sciencedirect.com/science/article/pii/S0364591602800062)
643 [S0364591602800062](https://www.sciencedirect.com/science/article/pii/S0364591602800062).
- 644 [61] van de Walle, A. Multicomponent multisublattice alloys, nonconfigurational entropy and other ad-
645 ditions to the Alloy Theoretic Automated Toolkit. *Calphad* **33**, 266–278 (2009). URL [https:](https://www.sciencedirect.com/science/article/pii/S0364591608001314)
646 [//www.sciencedirect.com/science/article/pii/S0364591608001314](https://www.sciencedirect.com/science/article/pii/S0364591608001314).

Figures

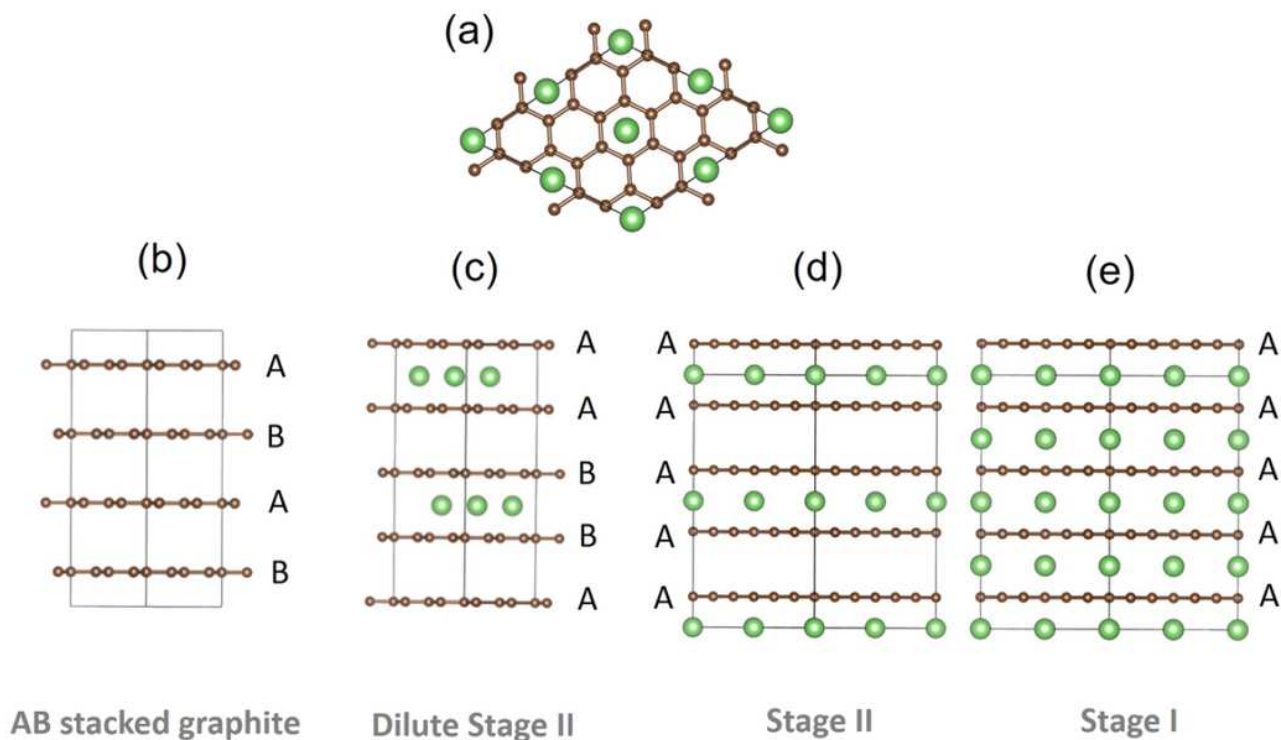


Figure 1

Structural representations of different carbon stackings in experimentally confirmed stages of graphite. (a) Top down view of carbon and lithium arrangements in Stages I and II. (b-e): side views, showing the layers occupied with Li and carbon stackings in (b) empty AB stacked graphite, (c) A α AB β B stacked dilute Stage II, with β indicating a lithium layer translated with respect to α , (d) A α AA α A Stage II and (e) A α stacked Stage I. Green represent Li atoms while the brown indicate C atoms.

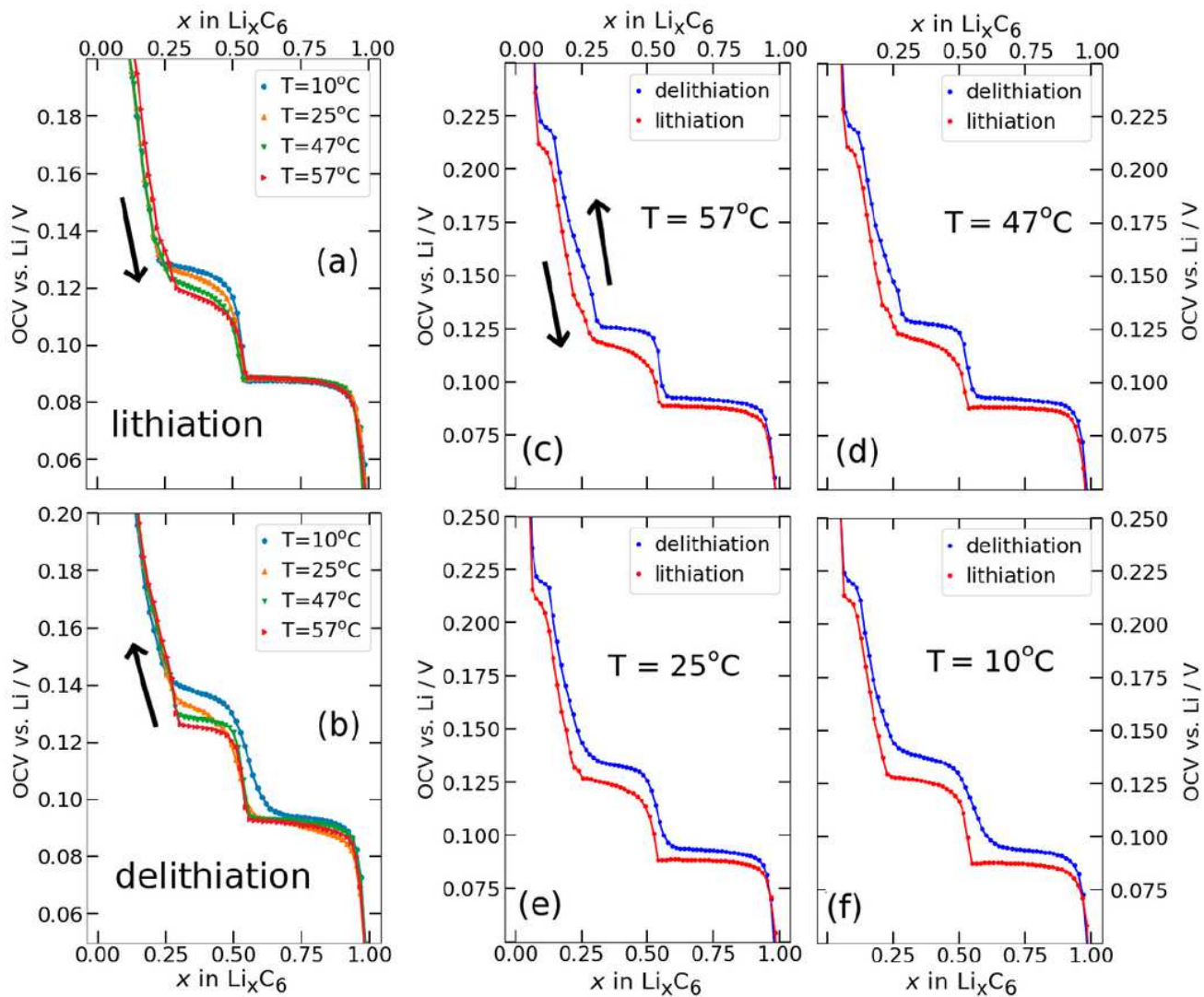


Figure 2

Experimental GITT results for (a) lithiation and (b) delithiation, at different temperatures, where the central cell temperature T_c is presented in the legend. Arrows indicate the direction of cycling. (c-f): the same results shown at fixed temperatures, in order of descending temperature (as indicated), with lithiation and delithiation overlaid.

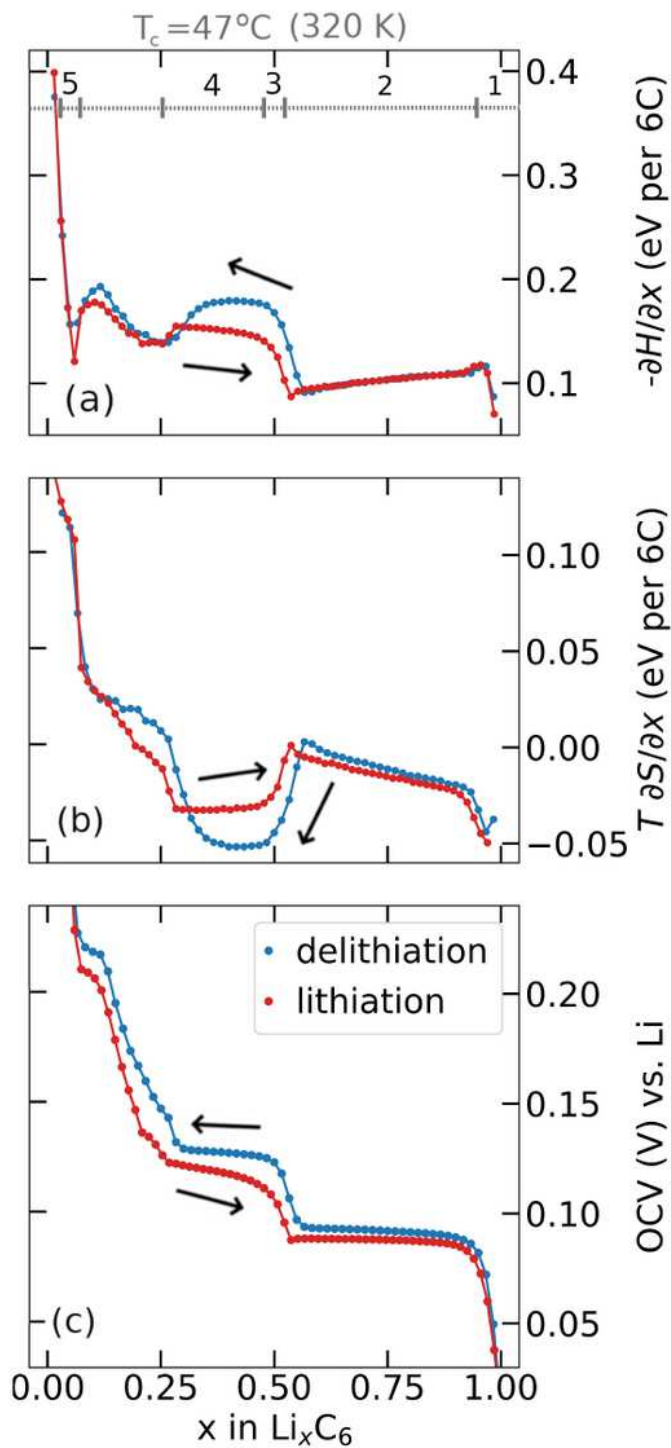


Figure 3

Proles obtained at central temperature, $T_c = 47^\circ\text{C}$: (a) partial molar (p.m.) enthalpy, (b) p.m. entropy and (c) open circuit voltage obtained during lithiation and delithiation (black arrows indicate direction of cycling), as a function of lithiation degree x in Li_xC_6 . The y-axis T in (b) is the absolute temperature expressed in degrees K, shown at the top of the column. Labelled features 1-5 corresponding to the lithiation profiles are referred to the main text.

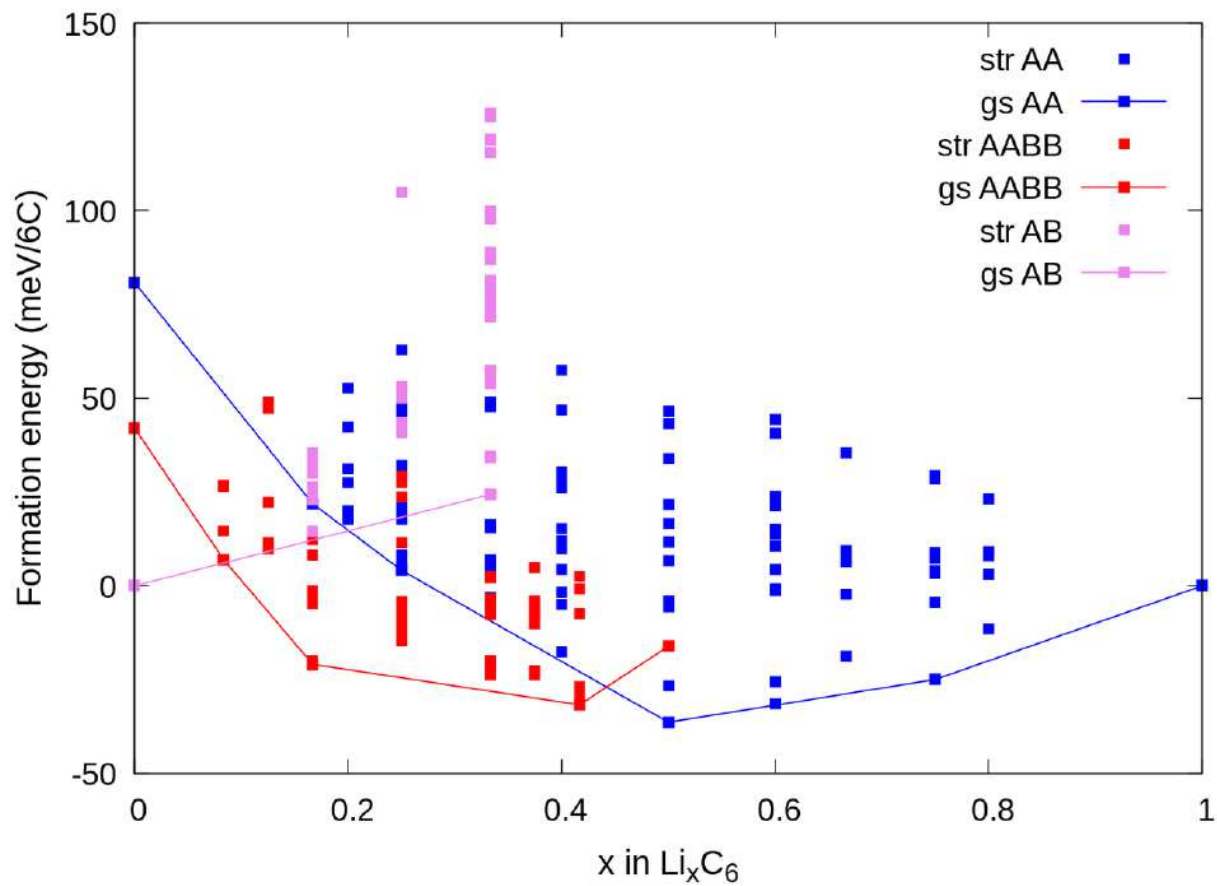


Figure 4

DFT calculations of ground state Li-graphite structures. Convex hull showing the formation energies (units meV/6C) of ground states from: blue line: stages I and stage II with AA carbon stacking; red line: dilute stage II with AABB carbon stacking; pink line: other dilute stage compounds with AB stacking. "str": structures sampled by cluster expansion; "gs": ground state structures.

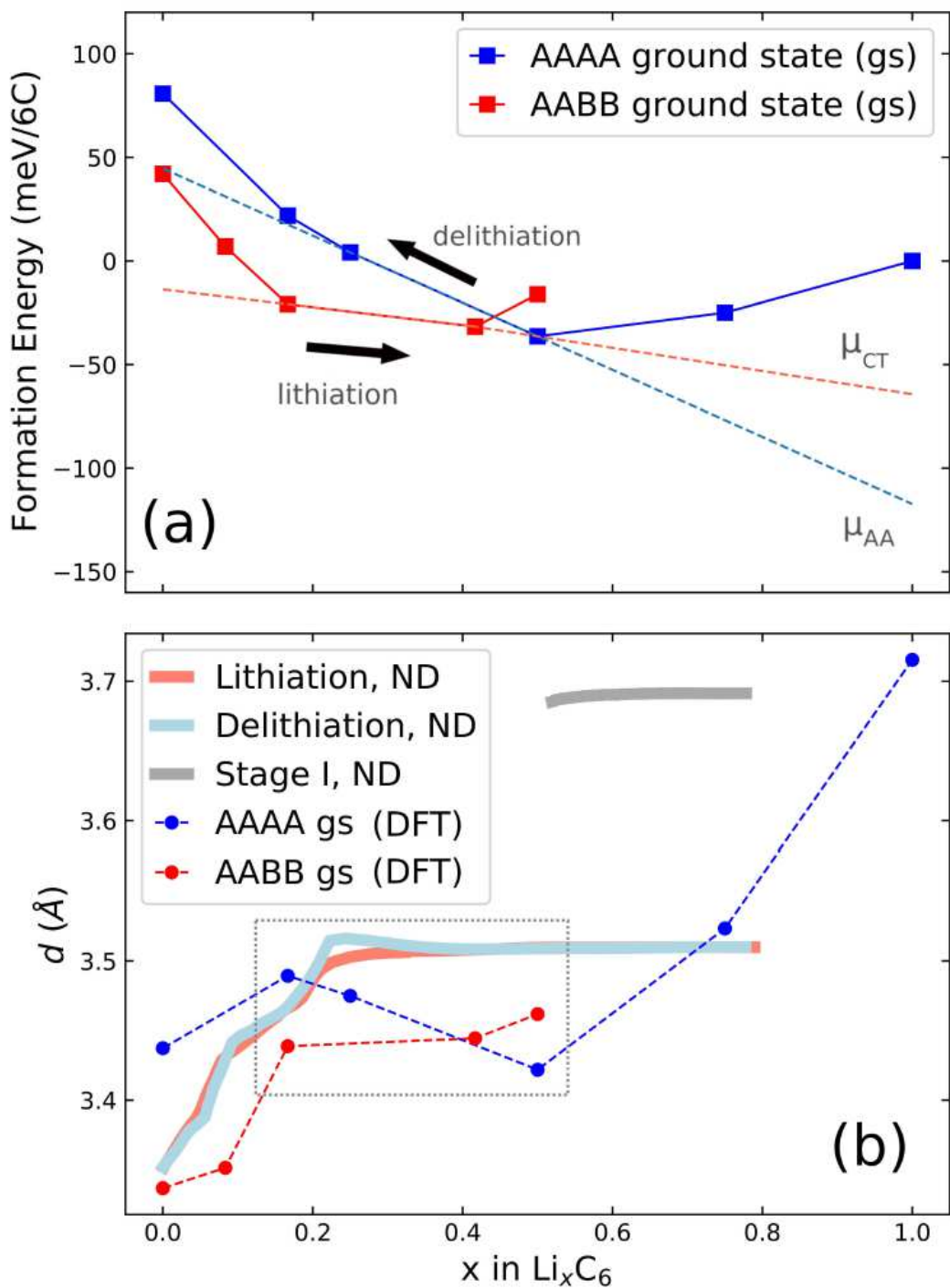


Figure 5

(a) Illustration of possible cycling pathways along the ground state (gs) free energy curves presented in Figure 4a. The slope of the red dashed line designates a chemical potential, μ_{CT} , which we propose is followed during lithiation. During delithiation, the AAAA-stacked structure persists as lithium is extracted from the host lattice, corresponding to chemical potential μ_{AA} . (b) Results obtained from neutron diffraction (ND) data. The average interlayer carbon distance, d , is shown as a function of lithium

concentration x . Reprinted (adapted) with permission from Fig. 1 of ref. [12]. Copyright 2020 American Chemical Society. d values obtained from the AAAA and AABB-stacked DFT ground states from the present work are overlaid for comparison.

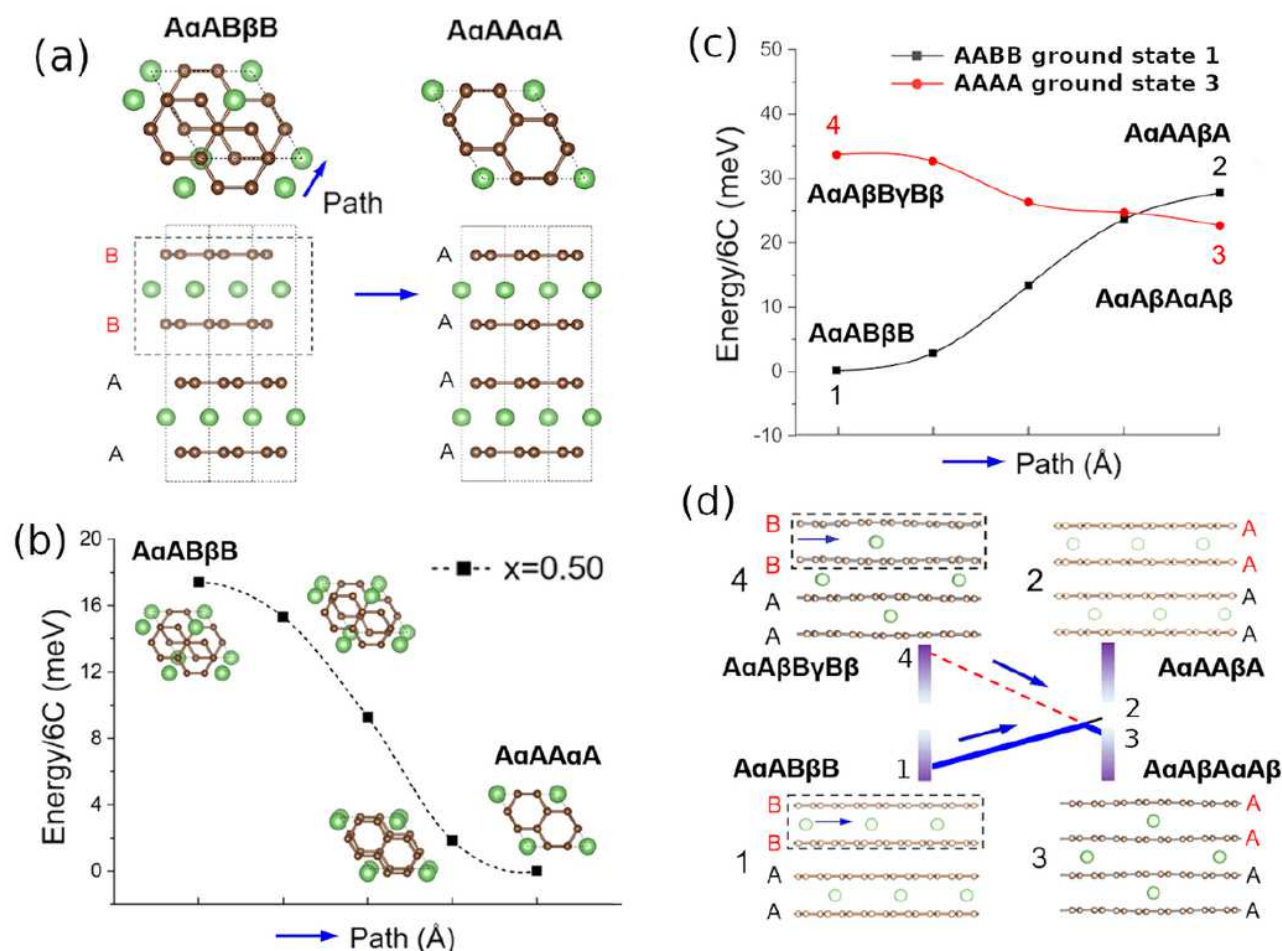


Figure 6

Nudged elastic band (NEB) calculations of layer translations. (a) Top down and side views representing the transition from AaABβB to AaAAaA stacking in the host lattice. The entire highlighted motif is translated along the indicated direction. (b) Energy profiles of transitions between AaABβB to AaAAaA host lattice stacking obtained at $x = 0.5$ (c) Energy profiles of stacking transitions at $x = 0.17$ using lattices based on the AaABβB ground state (denoted as 1) and AaAAaA ground state (denoted as 3), respectively. (d) Side views representing the carbon and lithium orderings at the two endpoints of the path. In (c) and (d) the notation indicates the lithium and carbon stackings at the two ends of the NEB path.

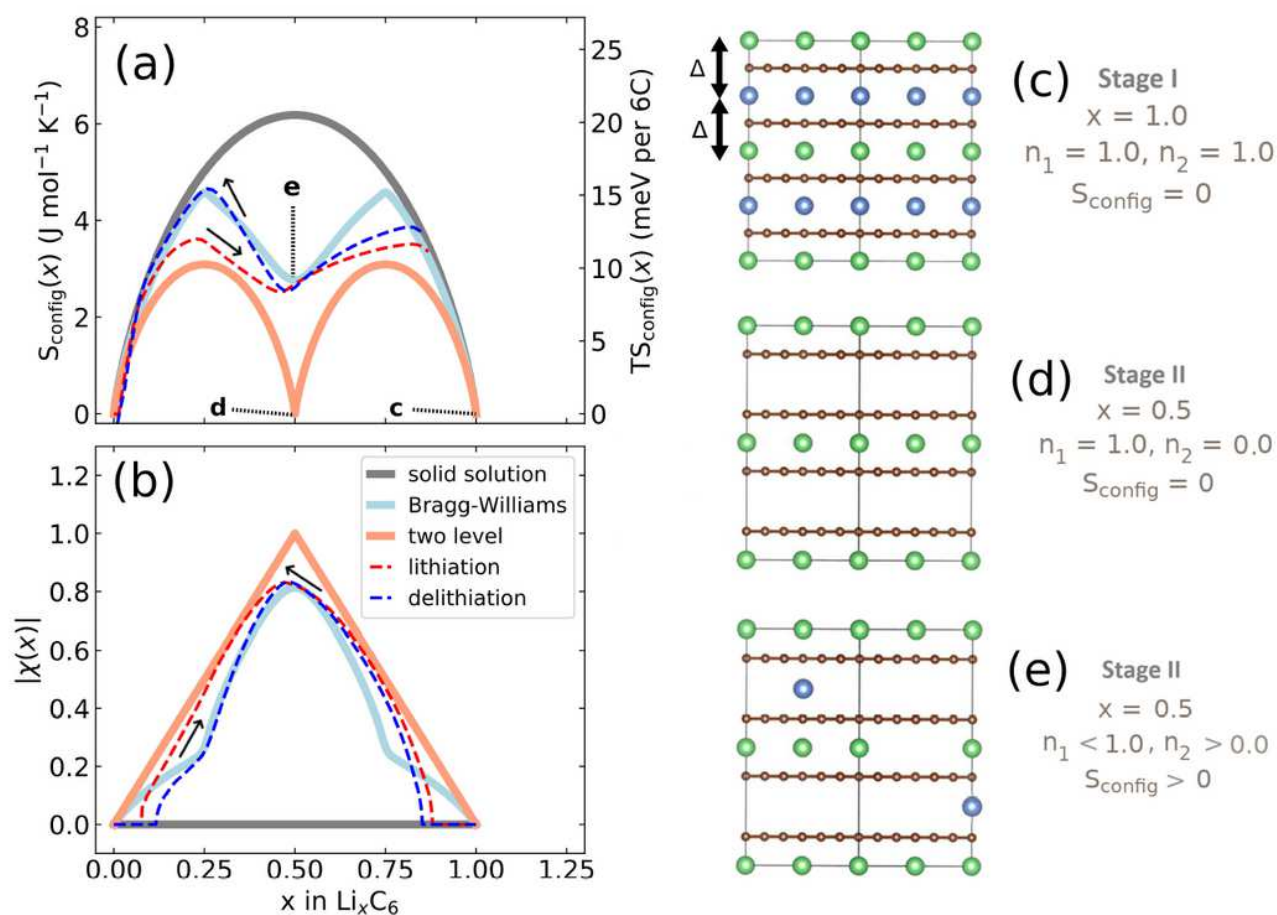


Figure 7

(a) Configurational entropy obtained at central temperature $T = 320$ K: dark grey solid line: ideal solid solution; light blue solid line: Bragg-Williams solution with interplanar mean field Li-Li repulsion of 75 meV; salmon solid line: sequential two level solid solution; red dashed line: experimental lithiation; blue dashed line: experimental delithiation. (b) Order parameter $|X|$, as described in the main text, labelled as in (a). In (a), select points (c-e) are indicated and schematic representations of the lattice occupations of Li in levels n_1 (green balls) and n_2 (blue balls) are shown on the right.

Supplementary Files

This is a list of supplementary files associated with this preprint. Click to download.

- [supplemental.pdf](#)